

THE INFLUENCE OF MICROSTRUCTURE ON THE STRENGTH
AND ELECTRICAL CONDUCTIVITY OF DIRECTIONALLY SOLIDIFIED
Cu-Ag MICROCOMPOSITES

By

KEUN YONG SOHN

A DISSERTATION PRESENTED TO THE GRADUATE SCHOOL
OF THE UNIVERSITY OF FLORIDA IN PARTIAL FULFILLMENT
OF THE REQUIREMENTS FOR THE DEGREE OF
DOCTOR OF PHILOSOPHY

UNIVERSITY OF FLORIDA

1997

To my wife, children, and parents

ACKNOWLEDGMENTS

I would like to express my deepest appreciation to God Who has been always leading my life with endless love, endurance, and benefits even when I did not realize it. He willingly became a shelter whenever I struggled with every type of "storm" and a shade for all kinds of "strong rays". He was always there wherever and whenever I needed.

I would also like to thank to all the persons who helped me directly and indirectly through the course of this work. Especially, my committee chairman, Dr. Michael J. Kaufman, has provided me with much encouragement, confidence, friendship, and support. At the times, whenever I was out of focus, he led me to the right way. His timely comments together with technical advice were invaluable.

I am also very thankful to Dr. Fereshteh Ebrahimi for her advice on mechanical property evaluation and continued interest in this work. I would also like to thank to Dr. Reza Abbastian, Dr. Robert T. DeHoff, and Dr. Ashok V. Kumar for their valuable comments and advice.

I am also grateful to our group members who helped me in various way so frequently. I thank to Dr. Vladimir Levit, who arranged for me to use the experimental system and gave me good comments. I also thanks to Mr. Verlyn Fisher and Mr. Victor Miller in the National High Magnetic Field Laboratory (NHMFL), who arranged and helped me to use drawing machine under their tight schedule.

Finally, with all my heart, I am especially grateful to my wife Kwang-ok for her warm and heartfelt but hidden assistance. Her sacrifice with patience and unconditional love during the many stressful moments was the basis of this completion. I would also like to share this achievement with my daughter Yewon and my son Insup.

TABLE OF CONTENTS

	page
ACKNOWLEDGMENTS.....	iii
ABSTRACT.....	vii
 CHAPTERS	
1. INTRODUCTION.....	1
2. LITERATURE REVIEW.....	4
2.1 Why High Magnetic Fields?.....	4
2.2 What Is a Pulsed Magnet?.....	4
2.3 Material Requirements for Pulsed Magnets.....	6
2.4 Classification of High-Strength, High-Conductivity Alloys.....	8
2.5 Cu-Ag Alloys : A New Look at an Old System.....	13
2.5.1 Why Cu-Ag?	13
2.5.2 Previous Work on Cu-Ag System.....	18
2.5.3 Strengthening Model of Cu-X Microcomposites.....	21
3. EXPERIMENTAL PROCEDURE.....	27
3.1 Specimen Preparation.....	29
3.1.1 Solidification.....	29
3.1.2 Deformation Processing.....	29
3.1.3 Heat Treatment.....	29
3.1.4 Initial Orientation Determination.....	30
3.2 Characterization.....	30
3.2.1 Microstructure.....	30
3.2.2 Mechanical Property-Tensile Test, Hardness.....	30
3.2.3 Electrical Conductivity.....	31
4. RESULTS AND DISCUSSION.....	33
4.1 Influence of the Volume Fraction of Eutectic Constituent.....	33
4.1.1 Microstructure.....	34
4.1.2 Strength.....	38
4.1.3 Conductivity	47

4.1.4 Strength-Conductivity Factor.....	48
4.2 Influence of Interlamellar Spacing.....	53
4.2.1 Microstructures.....	53
4.2.1.1 As-solidified structure.....	53
4.2.1.2. As-deformed structures.....	54
4.2.2 Strength.....	59
4.2.3 Conductivity.....	60
4.2.4 Strength-Conductivity Factor.....	65
4.3 Influence of Initial Orientation of Lamellae.....	66
4.3.1 Microstructure.....	66
4.3.2 Strength.....	72
4.3.3 Conductivity.....	72
4.3.4 Combination of Strength and Conductivity.....	77
4.3.5 Other Considerations.....	83
4.4 Influence of Growth morphology of Interdendritic Eutectic.....	83
4.4.1 Microstructure.....	87
4.4.1.1 As-solidified structure.....	87
4.4.1.2 As-deformed structures.....	94
4.4.2 Strength and Conductivity of DS Alloys.....	101
4.4.2.1 Strength.....	101
4.4.2.2 Conductivity	105
4.4.2.3 Strength and conductivity.....	108
4.5 Influence of Precipitation.....	112
4.5.1 Peak Hardness Identification.....	112
4.5.2 Aging Behavior and Prestrain Effect.....	117
4.5.3 Microstructure.....	120
4.5.4 Influence of Precipitation on Strength.....	123
4.5.5 Influence of Precipitation on Electrical Conductivity.....	125
4.6 Influence of Composition.....	126
5. CONCLUSIONS.....	133
5.1 Influence of the Volume Fraction of Eutectic Constituent.....	133
5.2 Influence of Interlamellar Spacing (λ) of Eutectic.....	134
5.3 Influence of Initial Orientation of Lamellae.....	135
5.4 Influence of Growth Morphology of Interdendritic Eutectic.....	135
5.5 Influence of Precipitation.....	137
5.6 Influence of Composition.....	137
LIST OF REFERENCES.....	138
BIOGRAPHICAL SKETCH.....	149

Abstract of Dissertation Presented to the Graduate School
of the University of Florida in Partial Fulfillment of the
Requirements for the Degree of Doctor of Philosophy

THE INFLUENCE OF MICROSTRUCTURE ON THE STRENGTH
AND ELECTRICAL CONDUCTIVITY OF DIRECTIONALLY SOLIDIFIED
Cu-Ag MICROCOMPOSITES

By

Keun Yong Sohn

May, 1997

Chairman: Michael J. Kaufman

Major Department: Materials Science and Engineering

An analysis of the interrelationships between microstructure and both mechanical and electrical properties in deformation-processed Cu-Ag alloys is presented. The effects of microstructure on the strength, electrical conductivity and strength-conductivity combinations were evaluated to provide guidelines for property optimization. Different microstructures were prepared by varying (a) the growth conditions during directional solidification, (b) alloy composition, (c) deformation level, (d) lamellar orientation and (e) thermomechanical processing schedule. The increased interfacial area of the eutectic structure is shown to result in a more rapid decrease in conductivity during deformation when compared with those alloys with considerable volume fractions of the primary

phase. As the initial interlamellar spacing becomes smaller, the hardening rate is not changed while the conductivity of the eutectic alloy decreases more rapidly with deformation. Both lamellar and rod-like eutectics were investigated and the resulting structures and properties after deformation were considerably different. The dominant factors determining the value of the strength-conductivity factor (SCF), where the SCF is the ratio of the ultimate strength to the conductivity are the volume fraction, interlamellar spacing, morphology and orientation of the Cu-Ag eutectic.

CHAPTER 1

INTRODUCTION

Materials for high field magnets for pulsed-field applications have been of recent interest because of their potential applications in many industrial fields [1-3]. The generation of the strong magnetic fields for pulsed magnets requires a material with high electrical conductivity to minimize Joule heating and high strength to withstand the Lorentzian forces exerted during the pulse. *In-situ* processed microcomposites, such as those produced in Cu-Nb and Cu-Ag alloys, provide better combinations of strength and conductivity than macrocomposites such as Cu/SS (stainless steel) and Cu/Ti [4, 5]. Furthermore, the submicron microstructures typical of these microcomposites enhance the strength beyond the rule of mixtures values predicted from the constituent phases [6-8].

Of the many Cu-X microcomposites studied, Cu-Nb alloys have been investigated the most intensively over a wide range of deformation levels and microstructures [6, 8-34]. Although high strength levels can be achieved in deformation-processed Cu-Nb microcomposites, their conductivity falls short of the level required for high field magnets.

In 1991, Sakai and coworkers [35] reported enhanced properties in a Cu-Ag alloy as compared with those of the Cu-Nb alloys that had been studied extensively. One of the reasons for the better strength and conductivity is related to precipitation of Ag from the

Cu phase during thermomechanical processing treatments (TMP). The TMP treatments enhance precipitation of solute atoms producing fine precipitates distributed uniformly throughout the matrix. However, they used several intermediate heat treatments with no explanation for the selected times, temperatures and prior deformation levels. A more quantitative understanding of the effects of the different microstructures including the size and distribution of precipitates is necessary for process and property optimization.

Besides interface strengthening in the two-phase structures, several strengthening mechanisms are involved in the Cu-Ag system, including solid solution hardening, precipitation hardening, and strain hardening. While the strength can be increased via these mechanisms, they cause a concurrent decrease in electrical conductivity and little has been done to optimize this combination of properties. Of the several strengthening mechanisms, it is not well established which mechanism is most effective in increasing strength with only a minimal decrease in conductivity. This is probably due to the limited work that has been done on the analysis of the interrelationships between the microstructure and both the mechanical properties and the electrical conductivity. Therefore, more systematic studies are necessary to specify the microstructure-property relationships in this alloy system.

The purpose of this work is to evaluate the influence of microstructural changes on the strength and electrical conductivity and thereby provide guidelines for property optimization. Different microstructures were prepared by varying (1) the growth conditions during directional solidification (DS), (2) the alloy composition, (3) the deformation level and (4) the TMP history. Both directionally solidified and conventionally solidified (CS) ingots were compared and contrasted after various

processing steps in order to determine the influence of microstructural changes on both the mechanical and electrical properties.

CHAPTER 2 LITERATURE REVIEW

2.1 Why High Magnetic Fields?

High magnetic fields are becoming more useful for the detailed characterization of materials. The higher the magnetic field, the better the resolution of the system for the characterization of a material's structure [3]. Many researchers in condensed matter physics or medical diagnosis fields utilize high magnetic fields as in magnetic resonance imaging (MRI) or nuclear magnetic resonance (NMR) systems. The MRI application, especially, represents a \$10 billion industry in the 1990s [1]. In addition, magnetic levitation for high-speed mass transport and superconducting magnetic energy storage (SMES) for storing and redistributing electrical power are other applications of high magnetic fields.

2.2 What Is a Pulsed Magnet?

High magnetic fields are generated by two methods: superconducting and resistive conductor technologies [1, 2, 36-47]. Superconducting solenoids can generate continuous fields up to 20T (tesla, 1T=10000 Gauss), which is known to be the present upper limit of performance with available superconductors [4, 40, 44]. A hybrid magnet system, which uses both resistive and superconducting technologies to produce continuous fields up to 45T in its bore, is being developed at the National High Magnetic Field Laboratory

(NHMFL) in collaboration with the Francis Bitter National Magnet Laboratory (FBNML). Currently, induction fields in excess of 50T can only be produced in pulsed magnets in which pulses are generated by energy discharged into a resistive solenoid [36]. The pulsed magnet systems can generate higher magnetic fields at relatively lower cost and are easy to construct.

Pulsed magnets can be classified into four categories depending on their pulse duration and field strength as shown in Table 1 [38, 48]. The first three types are nondestructive in that they are not expected to be destroyed during the pulse. At present, pulsed magnets designed to generate more than 100T are destructive, that is, the coil and the experimental set-up are destroyed due to the field generated for ultrashort periods and the characteristics of the technique used [38]. In this destructive system, the maximum field varies from shot to shot and the duration of the field pulse is generally in the microsecond range. These unstable fields may result in serious errors in the scientific data obtained due to the difficulty in controlling the process. For application to scientific measurements, it is desirable to have nondestructive magnets with longer pulse durations [49]. Ideally, the magnet itself should not be destroyed since repeated use of the system is desirable and the sample may need to be preserved due to its unique characteristics. In addition, long pulse or quasi-stationary fields are desired to establish thermodynamic equilibrium in the sample because the field pulse induces eddy currents and heats the sample. The ultimate goal is to produce a nondestructive pulsed magnet with a field induction of 100T for about 1 second [36, 50].

Table 1. Classification of pulsed magnets in terms pulse duration, field strength, and magnet life [38, 48].

Type	Pulse Duration	Field Strength	Remarks
Long (quasi-stationary)	100 ms-1 s	30-60T	Nondestructive
Standard	10-100 ms	40-70T	Nondestructive
Short	100 μ s	70-80T	Nondestructive
Ultrashort	0.1-5 μ s	>100T	Destructive

2.3 Material Requirements for Pulsed Magnets

The main factor limiting the maximum field to be generated in a nondestructive pulsed magnet is the tensile strength of the material used in the coil of the magnet [49, 51]. The maximum, tensile, hoop stress (σ_{\max}) in the plane of the innermost coil shell induced by the Lorentz force is proportional to the square of the field strength (B), shown in the constant hoop stress model [36, 49] as follows:

$$B = \sqrt{2\mu_0 \ln \alpha} \sqrt{\sigma_{\max}} \quad (2-1)$$

where μ_0 is the magnetic permeability of a vacuum and α is the ratio of the outer to the inner diameter of the solenoid. As the magnetic field increases, the energy density in the shell becomes very high, which causes a burst of the coil of the solenoid. Figure 1 [36] shows that 100T could be achieved even with hard drawn copper as the conductor, but a 10 mm bore (inner diameter) would require an outer diameter of 10 km, because the

attainable field scales with $\sqrt{\ln \alpha}$. Therefore, increasing the strength of the conductor allows the construction of magnets which are simpler, smaller and more efficient. Recent models show that it is possible to achieve field strengths of 100T using conductors with 1.5-2 GPa UTS (ultimate tensile strength) at reasonable coil dimensions [52].

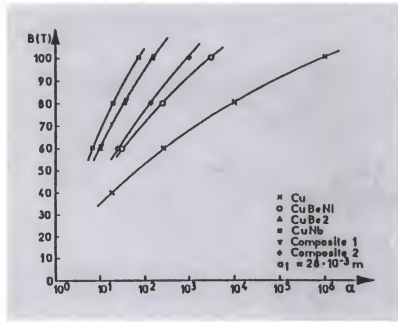


Figure 1. Magnetic field as a function of coil dimension, α , for different materials [36].

However, the high strength must be combined with high electrical conductivity to minimize the temperature rise due to the heat generated in the resistive coil during the pulse. A 70T magnet is estimated to experience electrical current densities of about 3 kA/mm² which is enough to cause substantial Joule heating even in pure copper [52]. Precooling the magnet to 77K before operation is used to reduce the temperature excursion, but the coil would still be heated up to over room temperature during a pulse. The conductivity of the conductor is, therefore, a critical factor in determining the pulse

duration. Unfortunately, the electrical conductivity usually varies inversely with strength and, therefore, any strength increase results in a conductivity decrease. High strength wires with low conductivity (<50% IACS) such as stainless steel or CuBe are not useful because they allow only extremely short pulse durations [49]. These two properties are thus the prime requirement of resistive conductors in high field pulsed magnets.

The high strength conductor should also have reasonable ductility so that it could be processed into wire and deformed around a winding mandrel in coil form without cracking. The minimum required elongation to failure is estimated at about 5% [53]. A high heat capacity is also desirable in order to absorb the heat generated during the pulse and a high thermal conductivity is necessary to insure a more uniform temperature distribution during and after the pulse. Because the electrical conductivity is a function of temperature, the non-uniform temperature distribution results in "hot spots" which can lead to further localized heating and ultimate failure [52]. In addition, the conductor needs to have good fatigue resistance, low thermal expansivity, and be reasonably low in cost.

2.4 Classification of High-Strength, High-Conductivity Alloys

There are two types of high-strength, high-conductivity materials being used for pulsed magnets: macrocomposites and microcomposites. Table 2 lists some of the high strength, high conductivity alloys. Macrocomposites normally consist of pure copper shielded with a reinforcement material, where pure copper carries most of the electrical conduction and the shielding material supports the copper conductor. Copper/stainless

steel is one of the more popular composite conductors of this type [54]; these are fabricated by inserting a pure copper core into a stainless steel tube followed by swaging and drawing to final dimensions with intermediate annealing treatments. The properties of the macrocomposites are in good agreement with the rule of mixtures where the properties scale with the relative volume fractions of each component [5]. Thus, both the strength and conductivity can be predicted from the cross-sectional areas and volume fractions of each component. Macrocomposites, however, have a relatively low combination of strength and electrical conductivity when compared with microcomposites as shown in Table 2. This is because the reinforcement material contributes only a small portion to the total conductivity due to its higher resistivity whereas the copper core has a low tensile stress and reduces the overall strength. The other drawback of the stainless-steel-clad-copper conductor is its poor transverse thermal conductivity resulting from the low thermal conductivity of the stainless steel and its poor heat transfer at the interface between the copper and the reinforcement during the pulse. This limits the pulse duration and, consequently, this conductor is not suitable for long-pulse applications.

Microcomposite conductors, however, can be used for long-pulse magnets because of their *in-situ* production characteristics which provide more perfect heat transfer at the interphase interfaces providing for greater energy absorption. These composites are normally produced by casting and subsequent deformation processing to produce a copper matrix reinforced with fine scale filaments, whiskers or dispersoids of another material. The strengths of the microcomposites are much higher than those of the macrocomposites because they utilize several strengthening mechanisms such as solid

solution hardening, precipitation/dispersion hardening, work hardening as well as interphase interface hardening depending on the nature of the reinforcing materials. These strengthening characteristics of the microcomposite enhance the strength to levels exceeding those predicted by the rule of mixtures [6-8]. The strengths of the microcomposites are very dependent upon the volume fraction and strength of the second phase, the amount of cold work, the interphase interface structure, the inter-filament spacing, and the size and distribution of any precipitates.

There are several types of high-strength, high-conductivity Cu-X microcomposites including Cu-Cr [55-68], Cu-Ta [59, 64, 66, 69], Cu-Nb [6, 8-34], Cu-Mo [58], Cu-Fe [10, 65, 70-73], Cu-Be [74], Cu-V [10], Cu-Al₂O₃ ("GlidCop") [4, 75], and Cu-Ag [4, 5, 7, 16, 32, 35, 66, 76-93] alloys. Among these, the Cu-Nb system has been the most intensively studied for pulsed magnet applications during the past few decades. This material is produced by consumable arc melting followed by rod rolling and drawing. The resulting bcc niobium filaments act as effective barriers for dislocation movement across the interphase interface. Niobium is more ductile than other refractory materials so that it is co-deformed with copper more readily than, for example, tantalum during cold working although there are some differences in the deformation rate [34, 94]. These composites provide excellent strength with reasonable electrical conductivity at niobium contents of 15-20 volume%. Foner et al. reported a 68.4T field in a pulsed magnet made using a deformation-processed Cu-18vol%Nb alloy [95, 96].

In spite of the successes with Cu-Nb, there are some difficulties in the processing of these alloys. Because of the high melting point of Nb (2469°C), consumable arc melting appears to be the best approach for ingot preparation. Induction melting in a

Table 2. Room temperature strength and conductivity of pulsed magnet conductors.

Material	Condition	Mechanical Properties			Electrical Conductivity (%IACS)	References
		UTS (MPa)	YS (MPa)	El. (%)		
TP copper	Annealed	250	110	45	94.3	[4]
	Hard drawn	400	330	25	82	[4]

MACROCOMPOSITES**Cu/SS**

DCF95-316SS	52%Cu	600	540	1.1	73	[4]
DCF101-304SS	60%Cu	730	670	1.1	63	[4]
DCF 400-304SS		860	770		60	[26]
DCF 401-304		720	610		58	[26]
HEF4-304	60%Cu, 75%RA	870	700	1.8	64	[4]
HEF3-304	50%Cu, 70%RA	900	710	2.0	51	[4]
HEF1-321	60%Cu, 75%RA	800	430	2.0	66	[4]
CuBe/Cu	6h @300°C	930	765		52	[26]

Cu/Ti

CP125	Pure Ti, 98%RA	1140	890	7.6	-	[4]
TCC	30%Cu	680	590	6.3	45	[4]
IO	50%CU, 95%RA	770	470	6.5	60	[4]

MICROCOMPOSITES**Cu-Al₂O₃**

GlidCop Al-15f	C15715, 90%CW	537	506	12	93.4	[75]
GlidCop Al-60E	C15760, 70%CW	620	570	9.2	79.5	[75]
GlidCop ^R		474	412		87	[26]

Cu-Cr

Cu-15v/oCr (12.4wt%)	Extrusion+Drawing +Heat Treatment	1100			72.5	[62]
-------------------------	--------------------------------------	------	--	--	------	------

(Table 2-continued)

Cu-15v/oCr	Same, but lower strain	960			78	[62]
Cu-7v/oCr		890			81	[62]
Cu-Nb						
CU-5%Nb	Annealed	900			80	[25]
	Unannealed	950			70	[25]
Cu-20%Nb		1150			63	[25]
Cu-20v/oNb	I/M	1100			65.5	[24]
	P/M	1080			58	[24]
Supercon		990	650	3.2	76	[4]
Cu-18Nb	Supercon, wire	966	842	7.8	75.7	[29]
	Supercon, wire	1104	994	7.2	69	[29]
	Supercon, sheet	1082	966	4.9	66.5	[29]
Bochvar		1070	770	2.0	71	[4]
Cu-18vol%Nb		966			70	[95]
Cu-18vol%Nb		1173	1035	1.2	60	[96]
Cu-Nb-Ag						
Cu-7%Ag-12%Nb	Miscellaneous treatment	1273	1185	6.6	66.5	[90]
Cu-7%Ag-12%Nb	4-stage HT at 450 & 350°C	1123	900	8.1	69.8	[90]
Cu-Ag						
16%Ag		950	850	7.2	80	[4]
18%Ag		1020	950	2.9	80	[4]
24wt%Ag	As-cast	275		34	83	[86]
	As-cast+450°C-10h	330		16	96	[86]
	As-cast+450°C-10h +93%RA	1000			79	[86]
24wt%Ag	450°C-1h at 40, 70% RA	1000			80	[35, 97]
24wt%Ag	Sheet, 96%RA, 3HTs	1050			75	[91]

graphite crucible results in the reaction of carbon to form niobium carbides, which deteriorate the mechanical and electrical properties of the alloy. The use of the consumable arc melting technique limits the maximum available size of Cu-Nb ingots (<25kg) [29] and results in segregation of niobium causing inhomogeneous properties in the wire. Rebundling during drawing is usually necessary in order to obtain the desired refinement strain in the application-size wires [20, 29].

2.5 Cu-Ag Alloys : A New Look at an Old System

2.5.1 Why Cu-Ag?

One of the drawbacks in the Cu-Nb alloys is its relatively low conductivity at high strength levels as shown in Table 2. This is in spite of the fact that the solubility of niobium in copper is very low. Therefore, since solute elements tend to lower the conductivity of copper, a desirable addition is one which (1) has low solubility, (2) is easy to process (has similar deformation rate), (3) has high conductivity and (4) has high strength. Silver has the highest conductivity of the elements and has the least detrimental effect on the resistivity of copper of all the elements studied to date [98]. These observations suggest that Cu-Ag microcomposites might be ideal as high-strength, high-conductivity materials for pulsed magnets. In 1991, Sakai and coworkers [35] reported that they achieved 80%IACS (International Annealed Copper Standard, 100%IACS=1.7241 $\mu\Omega$ cm) at a tensile strength of 1 GPa, which is about 5-10%IACS higher than that of typical Cu-Nb alloys at similar strength levels.

The strength-conductivity combination for Cu-Ag, Cu-Nb and other competitive materials are compared in Figure 2. Clearly, the Cu-Ag alloys represent the highest strength and conductivity combinations.

Cu-Ag alloys are also easier to process than Cu-Nb alloys. The melting point of silver is relatively low, 961.9°C, and both elements have low affinity for carbon. Therefore, induction melting using a graphite crucible is possible for Cu-Ag alloys and provides good compositional homogeneity in the ingot, resulting from the vigorous mixing caused by the induction. This benefit resolves the size limitation of Cu-Nb alloys so that scaling up to commercial ingot sizes is available at relatively low expense. Another advantage of Cu-Ag alloys is their good ductility and formability. A low extrusion temperature of about 500°C and low extrusion ratio of about 9:1 is sufficient to break down the dendritic structure of induction-melted billets [4]. Furthermore, more than 99%RA by cold drawing can be performed without intermediate annealing.

Several strengthening mechanisms can be used to improve the strength of the Cu-Ag alloys. As shown in Figure 3 [99], the Cu-Ag diagram contains a simple eutectic. Although both elements are fcc, they have limited solubility in the other. The maximum solubility of silver in copper is 4.9 at% whereas for copper in silver it is 14.1 at% [100]. The eutectic reaction generally produces a lamellar structure of the two phases although the volume fraction of copper is near the typical boundary (~30%) between lamellar and rod-like structures. The interphase boundary acts as a barrier to dislocation movement during subsequent deformation processing; this increases the work hardening rate of the material. For a copper-rich hypoeutectic alloy, the microstructure consists of primary copper dendrites surrounded by interdendritic eutectic. The strength of the alloy depends

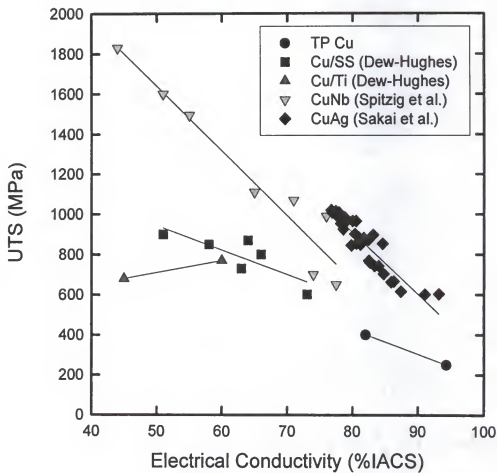


Figure 2. Strength and electrical conductivity of various alloys compared to a thermomechanically processed Cu-Ag alloy.

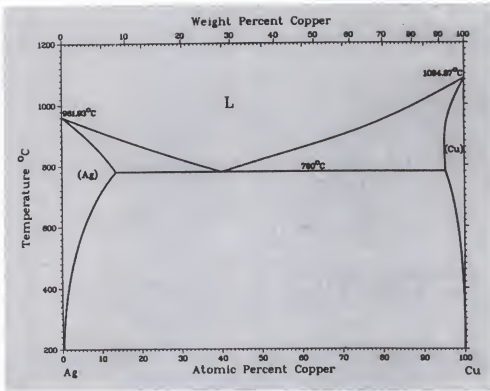


Figure 3. Alloy phase diagram of Cu-Ag system [101].

on the volume fraction and interlamellar spacing of the eutectic phase which depend on alloy composition and cooling rate, respectively.

Significantly, the solubility of one component in the other decreases on cooling to less than 0.2 at% at room temperature [100]. Thus, it is possible to utilize both solid solution strengthening and precipitation strengthening by applying appropriate TMP treatments in order to achieve the desired strength level. Since the lattice parameters of copper and silver are quite different ($a_{Cu}=0.3615$ and $a_{Ag}=0.4086$ nm), it is necessary to enhance precipitation of one phase in another by deformation processing prior to heat treatment. In addition, this system includes a metastable miscibility gap and continuous T_0 curves such that single phase formation by rapid solidification is possible [102-104];

the metastable single phase may undergo a spinodal decomposition on cooling or during subsequent heat treatment, depending on the composition range.

Since both the strength and conductivity are important, solid solution strengthening is not considered appropriate since solute atoms dissolved in the copper matrix reduce conductivity drastically while improving strength only moderately. The fine structures produced by rapid solidification processing (RSP) also have the drawback that the product is difficult to consolidate [60, 105]. Specifically, poor mechanical bonding between interlayers causes debonding during deformation processing and the high solute levels retained in the copper matrix during rapid solidification would presumably lower the electrical conductivity of the alloy.

Directional solidification is a useful tool for understanding the microstructural effects on the combination of both strength and conductivity in Cu-Ag microcomposites. Furthermore, by varying the composition and withdrawal speed, the microstructural scale, morphology, and volume fractions of the primary phases and the eutectic can be controlled to some extent. It also provides directionally aligned structures with which a study of the effect of the initial lamellar orientation on the properties is possible. For example, the unidirectionally aligned lamellar structure is stronger than random lamellar structures at similar interlamellar spacings when the stress is applied parallel to the lamellar direction.

By controlled directional solidification, it is also possible to grow off-eutectic compositions by coupled growth. For steady-state coupled growth of off-eutectic alloys, high thermal gradients, G_L , and low growth velocities, v , are required according to equation (2-2) [106] where:

$$G_L/v \geq -m_L(C_E - C)/D_L \quad (2-2)$$

where m_L is the slope of the liquidus line, C_E and C the eutectic and alloy compositions, respectively, and D_L the diffusivity in the liquid. This implies that compositions near the eutectic can be grown in a coupled fashion at reasonable rates whereas the maximum velocity for growth of off-eutectic compositions may be prohibitively slow. According to the above equation, it becomes more difficult to grow off-eutectic alloys as the composition becomes further removed from the eutectic.

There are some obstacles related to strengthening Cu-Ag alloys, namely, (1) silver is not as strong as the refractory metals Nb, Ta or Mo and (2) silver is fcc as is the copper matrix. In addition, pure copper and silver undergo dynamic recovery at high deformation levels even at room temperature [7]. The weak reinforcing nature and structural similarity of silver presumably limit the maximum available strength of the microcomposites. However, these facts may be overcome by a proper combination of precipitation hardening, interphase interface hardening and strain hardening. The Cu-Ag alloys have great potential for future applications as high-strength, high-conductivity materials and, thus, a full metallurgical investigation is highly desirable.

2.5.2 Previous Work on Cu-Ag System

Cline and Lee [78] investigated the effect of eutectic morphology on the high temperature strength of the specimens prepared by directional solidification. Two types of microstructures having different growth morphologies were prepared: lamellar and

equiaxed eutectic. The lamellar structures were as-solidified eutectic structures whereas the equiaxed structures were prepared by a recrystallization heat treatment following extrusion. Their results indicated that the alloy with the lamellar structure exhibited better high temperature strength than that of the equiaxed structure. The flow stress depended on the interlamellar spacing according to a Hall-Petch type relationship [77, 78].

Frommeyer and coworkers [7, 79, 107] showed that directionally solidified Cu-Ag eutectics revealed higher strength levels than the same alloy with similar interlamellar spacings produced by conventional casting. They also reported that the initial lamellar eutectic grown by directional solidification (DS) changed to a rod-like structure after severe deformation at a draw ratio of $\eta \sim 7$. The draw ratio is given by $\eta = \ln(A_0/A) = 2\ln(D_0/D)$, where A_0 and A are, respectively, the initial and final cross sectional areas and D_0 and D the initial and final diameters. They confirmed that the increased scattering of conduction electrons at the interface causes a strong conductivity decrease when the sizes of the copper and silver phases become comparable with the mean free path of the conduction electrons.

Much of the previous studies of Cu-Ag alloys dealt with the strengthening mechanisms in the lamellar structure and the microstructural evolution during rapid solidification processing [63, 102-104, 108-111]. Manna and Pabi [83, 84] observed an indication of discontinuous precipitation in a Cu-7.7at%Ag alloy. Hong and coworkers [32] also reported the presence of the discontinuous precipitation for thermomechanically-processed (TMP) Cu-Ag alloys. Although Embury [112] suggested that the discontinuous precipitation causes an increase in the work hardening rate due to realignment of the phases back along the wire axis during drawing, a further

understanding of the kinetics of this reaction is still necessary for determining the optimum thermomechanical process.

This alloy system has been of interest to researchers in high magnetic field generation since 1991 when Sakai et al. [35] reported 80% IACS at 1 GPa UTS in a Cu-16at%Ag after TMP. This was achieved by using intermediate heat treatments during the deformation processing. The property changes due to TMP are shown in Figure 4 where both the strength and conductivity were improved by TMP. TMP is a common procedure for Al-base alloys (e.g. Al-Li (8000-series)) that utilize precipitation hardening. The main purpose of this process is to increase the dislocation density in order to provide nucleation sites for those precipitates that are difficult to nucleate more homogeneously due to large lattice misfits. This process can greatly improve the strength and ductility of Al-Li alloys by distributing the fine precipitates (T_1 or S' -phase) uniformly throughout the matrix [113-115]. From the results of Sakai and coworkers, the conductivity increase is the result of the precipitation of solute atoms dissolved in the matrix [35, 86, 91, 97]. This is a reasonable explanation since the interphase interfacial area is decreased by the agglomeration of the dispersed solute atoms, because the interphase interface and the strain field around a solute atom are effective scattering sources for free electrons. Therefore, the increase in conductivity here is a "relative" increase. Precipitation does not necessarily result in an increase in both strength and conductivity. They attempted several intermediate heat treatments with no reasonable explanation for their selection. Thus, a more quantitative understanding of the effects of the different microstructures and the size and distribution of precipitates is necessary for process development.

2.5.3 Strengthening Model of Cu-X Microcomposites

As mentioned before, the deformation-processed, in situ Cu-X microcomposites exhibit strengths considerably above the values predicted by the rule of mixtures (ROM). These greater strengths are related to such microstructural factors as dislocation density, constituent, volume fraction of phases and distance between interphase boundaries. The crystal structures of the two phases are also important. In general, FCC-BCC combinations such as Cu-Fe [71], Cu-Cr [71], Cu-Nb [10] exhibit greater tensile strengths than FCC-FCC combinations such as Ag-Ni [71], Cu-Ag [7]. The reason for the greater strengthening in FCC-BCC alloys is due to the BCC filaments with ribbon-like cross sections that develop as a result of their developing {110} fiber texture during cold working [6].

Funkenbusch and Courtney [71] suggested a “geometrical dislocation” strengthening model in order to explain the strengths that develop in heavily deformed in situ composites. Specifically, these are geometrically necessary dislocations that develop in order to compensate for the differences in strain resulting from the different strength or stiffness of the two phases. According to Ashby [116], the average density of geometrical dislocations, ρ_G , in a polycrystalline grain is approximately expressed by:

$$\rho_G \approx K(\eta/D) \quad (2-3)$$

where η is the strain, D the grain size and K a geometrical constant which is a measure of the relative degree of mismatch among the polycrystalline grains. The above equation (2-3) was modified by Funkenbusch and Courtney [71] for the in-situ microcomposites as

follows:

$$\rho_G = 2K[1 - \exp(-\eta/2)]/D \quad (2-4)$$

While these geometrically necessary dislocations results from the strain inhomogeneities, statistical dislocations are generated as a result of random dislocation interactions within the crystal lattice. Assuming linear work hardening with deformation strain, the “statistical” dislocation density is proportional to η^2 . The variations of both types of dislocation density are plotted in Figure 5. At high strains, a very marked increase in ρ_G dominates the strength of the in-situ microcomposites.

Spitzig and coworkers developed an alternative “filament barrier” strengthening model where the filament spacing appears to be the primary source of strengthening in Cu-Nb microcomposites [94]. The strength of these materials is known to follow the Hall-Petch type relationship using the filament or interlamellar spacing, λ , instead of the grain size as follows [8, 77]:

$$\sigma = \sigma_0 + k(\lambda)^{-1/2} \quad (2-5)$$

where σ_0 is the intercept in the stress vs. λ plot and k is a constant which depends on the nature of adjacent phases.

During the deformation of these microcomposites, the mean filament or interlamellar (“barrier”) spacing is reduced in proportion to the wire diameter assuming no new barriers are generated or existing barriers destroyed. Therefore, the barrier

spacing as a function of strain is given by [117]:

$$\lambda_0/\lambda = D_0/D = \exp(\eta/2) \quad (2-6)$$

By combining equation (2-5) and (2-6), we obtain

$$\sigma = \sigma_0 + k(\lambda_0)^{-1/2} \exp(\eta/4) \quad (2-7)$$

Spitzig et al. modified the above equation by using their experimental data shown in Figure 6 on Cu-Nb alloys as follows[94]:

$$\sigma = \sigma_0 + k(\lambda_0)^{-1/2} \exp(\eta/5.6) \quad (2-8)$$

This equation indicates that the strength of the Cu-Nb microcomposites depends on both the draw ratio and the initial filament spacing in a manner similar to that observed in pearlite and eutectic composites [117, 118]. This result is not in accord with the usual interpretation that the high strength is a consequence of a high dislocation density or dislocation pileups at interfaces.

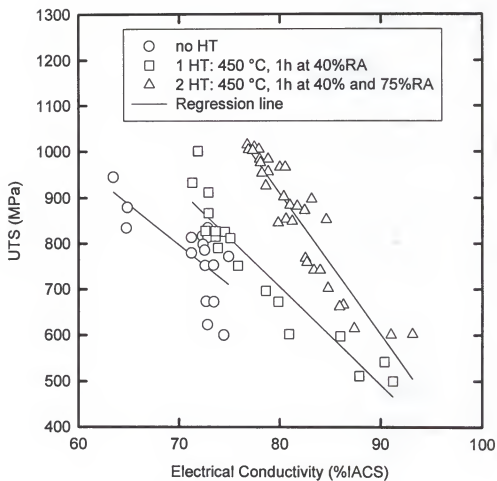


Figure 4. Property variation by TMP for chill-cast Cu-8~32at%Ag alloys [35].

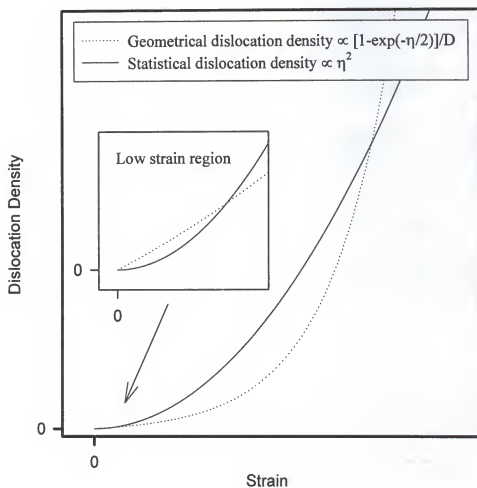


Figure 5. Schematic of statistical and geometrical necessary dislocation density in a two-phase composite as a function of deformation strain [71].

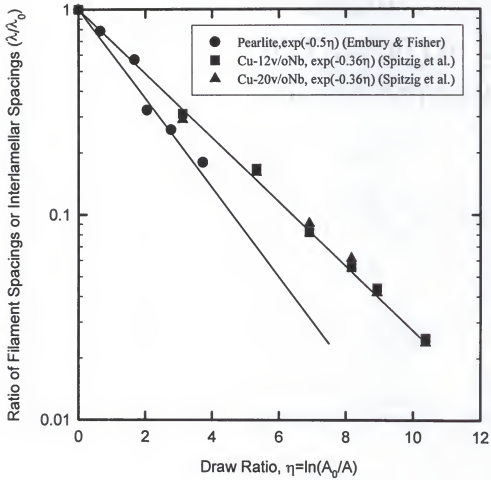


Figure 6. Effect of draw ratio on the Nb filament spacing (λ) in Cu-Nb microcomposites.

CHAPTER 3 EXPERIMENTAL PROCEDURES

In the Cu-Ag eutectic system, the strength and electrical conductivity of an alloy are characterized by the following microstructural factors:

- (1) Volume fraction of eutectic constituent
- (2) Interlamellar spacing (λ) of eutectic
- (3) Initial orientation of lamellae
- (4) Growth morphology of interdendritic eutectic
- (5) Size and distribution of precipitates
- (6) Amount of deformation

In order to study these features systematically, specimens were prepared by directional solidification and analyzed in terms of the following properties:

- (1) Strength vs. draw ratio (η)
- (2) Electrical conductivity vs. draw ratio
- (3) Strength vs. conductivity
- (4) Strain hardening rate
- (5) Heat treatment response of the above properties

In this manner, it should be possible to better quantify the relative importances of the different microstructural features and then make alterations for property optimization. The experimental procedure of this study is outlined in Figure 7.

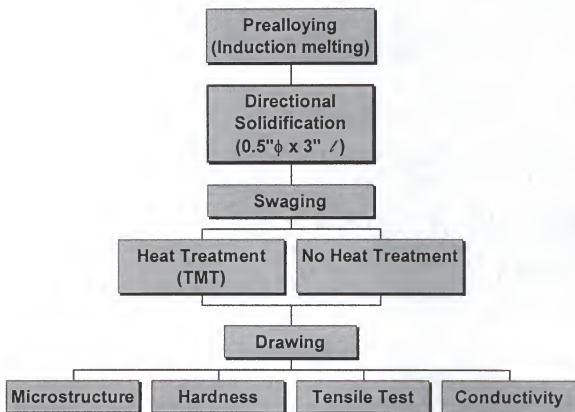


Figure 7. Flow diagram showing experimental procedures.

3.1 Specimen Preparation

3.1.1 Solidification

Cylindrical ingots of Cu-Ag alloys were prealloyed using silver shot of 99.99% purity and C101 copper rods (99.99% purity) by vacuum induction melting under a purified argon atmosphere. The pre-alloyed ingots were then placed in an alumina tube in contact with a water-cooled copper chill block at the bottom of a resistance furnace (Figure 8). After melting, the chill block and sample were withdrawn at speeds between 1.7 and 55 $\mu\text{m}/\text{sec}$ for directional solidification (Table 3). The bottom of the alumina tube was sealed with graphite in order to prevent the melt from leaking prior to solidification. A mechanical stirrer was attached at the top of the furnace and the melt was stirred manually prior to withdrawal in order to minimize the segregation resulting from gravitation and the nucleation nature of each phase. Conventionally solidified specimens were also prepared by vacuum induction melting under argon in a graphite crucible followed by pouring into a graphite mold.

3.1.2 Deformation Processing

The DS ingots were swaged to rods and then drawn to produce a true strain (η) of 6 or 7. Intermediate heat treatments were investigated in order to optimize the precipitation hardening effects in these alloys.

3.1.3 Heat Treatment

For the precipitation hardening studies, the ingots were heat treated at 720–750°C for 0.5–1 h and then water quenched to room temperature. The quenched specimens were

swaged to selected levels of deformation followed by artificial aging. The aging time and temperature were determined from the results of Vickers microhardness measurements on the specimens pre-aged under different conditions.

3.1.4 Initial Orientation Determination

For the study of lamellar orientation effects, three specimens with different lamellar orientations relative to one another (0° , 45° , 90° to the growth axis) were cut from the unidirectionally solidified ingots by electrodischarge machining (EDM). These specimens were then thermomechanically processed as indicated above.

3.2 Characterization

3.2.1 Microstructure

The microstructures of the as-solidified DS ingots were examined using light optical microscopy and scanning electron microscopy in the polished and etched condition. Transmission electron microscopy was carried out in order to resolve the fine microstructures of the deformation-processed specimens. For the TEM analysis, thin sections of the wire were prepared by argon ion milling after mechanical dimpling. In order to minimize the effect of heat generated during ion-milling, a liquid nitrogen cooled sample stage was used.

3.2.2 Mechanical Property Studies

Room temperature tensile tests were carried out using an Instron machine (Model 1125) with a crosshead speed of 1.27 mm/min in order to investigate the strength of the

drawn wires. The test specimens were machined from wires that were larger than ~1.3 mm in diameter. For diameters smaller than 1.3 mm, the tests were conducted by directly inserting the wire ends into Instron grips with smooth surfaces as indicated in ASTM E8-93. The strength of the materials was plotted as a function of draw ratio, η

3.2.3 Electrical Conductivity

Room-temperature, electrical-resistivity measurements were made using the four-point probe method on specimens of fixed length with input currents between 100 mA and 1 A. The potential differences at a given span were measured using a high sensitivity nanovolt meter (Keithley model 182).

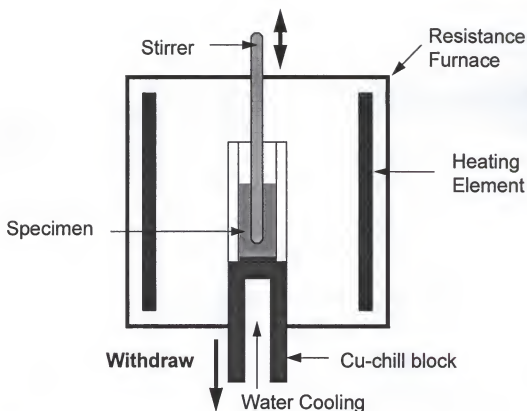


Figure 8. Schematic of the directional solidification apparatus.

Table 3. Alloy compositions and solidification rates for the DS alloys.

Specimen ID	Nominal Composition (at%Ag)	Withdrawal speed ($\mu\text{m}/\text{sec}$)	Dimension (mm)
DS 10	10	55	$10.7^{\text{d}} \times 75^{\text{f}}$
DS 55	55	1.7	$10.7^{\text{d}} \times 75^{\text{f}}$
DS 58	58	55	$10.7^{\text{d}} \times 75^{\text{f}}$
		12	$13.0^{\text{d}} \times 65^{\text{f}}$
DS 60	60	55	$5.8^{\text{d}} \times 75^{\text{f}}$
		2.5	$13.0^{\text{d}} \times 90^{\text{f}}$
DS 65	65	1.7	$10.7^{\text{d}} \times 75^{\text{f}}$
CS 58	58	-	$12.5^{\text{d}} \times 95^{\text{f}}$

CHAPTER 4

RESULTS AND DISCUSSION

4.1 Influence of the Volume Fraction of Eutectic Constituent

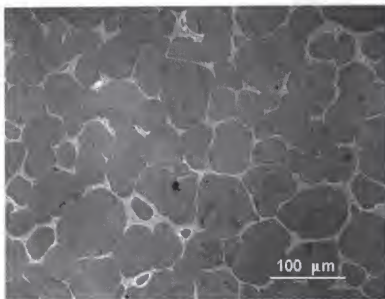
The interphase interface is a two-dimensional planar defect which either hinders or blocks a dislocation moving across the boundary. Therefore, higher volume fractions of the eutectic are expected to lead to higher strengths in these alloys. This does not necessarily mean, however, that alloys with high eutectic volume fraction will exhibit a better combination of strength and conductivity.

In this section, two alloys with different eutectic volume fractions were prepared and investigated: a eutectic alloy (Cu-58a/oAg) and a copper-rich alloy (Cu-10a/oAg). By plotting UTS (σ) against draw ratio (η), it is possible to determine how strength varies with draw ratio and how the hardening response ($d\sigma/d\eta$) varies with eutectic volume fraction. Both the strength and conductivity were quantified in terms of the interlamellar spacings of the eutectic. The conductivity vs. draw ratio plot provides the relative importance of the interphase interface area on the electrical conductivity. The degree of contribution of the interphase interfaces to both the strength and the conductivity will determine the usefulness of the interface in improving this combination of properties. This may be deduced from the slope of the strength vs. conductivity plot which reflects the effective strength increase for a given amount of conductivity reduction.

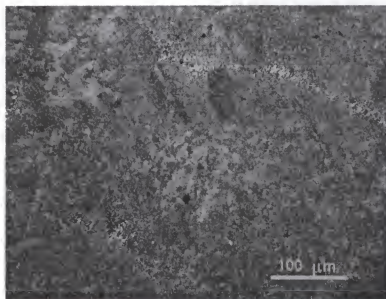
4.1.1 Microstructure

The as-cast microstructures of DS Cu-10a/oAg (DS 10) and Cu-58a/oAg (DS58) alloys are shown in Figures 9 through 11. The dark, round regions in Figure 9 (a) are primary copper dendrites and the lighter regions correspond to the interdendritic eutectic. The volume fraction of the primary copper in the DS 10 alloy is estimated to be about 89% from the lever rule applied to the Cu-Ag phase diagram. The DS 58 alloy shown in Figure 9 (b) does not contain primary copper although the compositions slightly hypoeutectic (Cu-rich) according to the phase diagram. From equation (2-2) described in the previous section, it is clear that compositions near the eutectic can be grown in a coupled fashion at reasonable rates whereas the maximum velocity for growth of compositions further from the eutectic composition may be prohibitively slow. Although the amount of undercooling was not measured in this study, the microstructure of the Cu-58Ag alloy shown in Figure 9 (b) reveals uniformly-developed lamellae of Cu and Ag, indicating that coupled growth was achieved at the solidification rate of 55 $\mu\text{m}/\text{sec}$. Figure 10 (a) is a polarized view of the transverse section through the DS 58 alloy grown at a withdrawal speed of 55 $\mu\text{m}/\text{sec}$. Small lamellar aggregates are observed and each colony has different lamellar orientations as shown in Figure 10 (b).

A longitudinal section of the DS 58 alloy reveals eutectic colonies aligned parallel to the growth axis (Figure 11 (a)). Each colony is mostly lamellar in nature with most of the copper and silver plates aligned parallel to the growth direction (Figure 11 (b)).

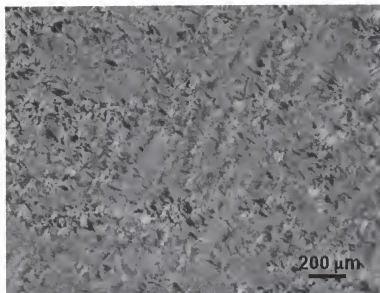


(a) DS 10

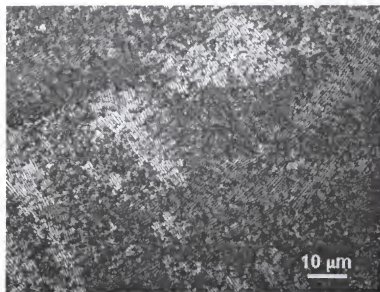


(b) DS 58

Figure 9. Optical microstructures of the as-cast DS 10 and DS 58 alloy.
($v=55 \mu\text{m/sec}$, transverse section, etched)



(a)



(b)

Figure 10. Optical microstructures of the as-cast DS 58 alloy.
($v=55 \mu\text{m/sec}$, transverse, etched, polarized light)

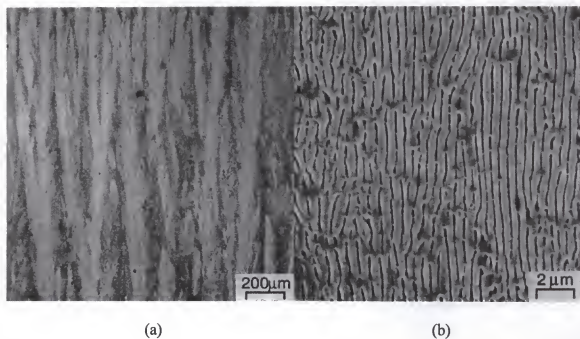


Figure 11. Optical (a) and SEM (b) microstructures of longitudinal section of the as-cast DS 58 alloy ($v=55 \mu\text{m/sec}$, etched). In (b) the light majority phase is silver.

4.1.2 Strength

In the barrier model for in-situ microcomposites, the UTS, σ , can be correlated with the filament or interlamellar spacing as [8, 77, 117]:

$$\sigma = \sigma_0 + k(\lambda)^{-1/2} \quad (2-5)$$

Figure 12 represents the strength dependence of the DS 58 eutectic alloy on interlamellar spacing. The regression line through the data points is described by:

$$\sigma = 297 + k(\lambda)^{-1/2} \quad (4-1)$$

The constant k , known as the Hall-Petch slope in the above equation, has a value of $0.17 \text{ MN/m}^{3/2}$, which is a little higher value than that ($k=0.14$) of the DS 60 eutectic alloy reported by Cline et al. [77]. These k values obtained from the Cu-Ag alloys are much lower than those of the Cu-Nb microcomposites where k has about $1 \text{ MN/m}^{3/2}$ [94]. This result supports the fact that k is greater in the composites where the two phases have different crystal structures (FCC-BCC). Although the structure of both phases are similar, the k value appears to depend on the strength of the neighboring phase considering the fact that drawn, pure copper has a k value of about $0.22 \text{ MN/m}^{3/2}$ [119] where the grain size is substituted for λ .

The variation in interlamellar spacing with draw ratio for the DS 58 alloy is shown in Figure 13. The regression line through the data points can be expressed by

$$\lambda/\lambda_0 = \exp(-0.40\eta) \quad (4-2)$$

This equation reflects that the reduction in interlamellar spacing is not exactly proportional to the reduction in the wire diameter assuming that no new barriers are created or existing barriers destroyed. These variations in the interlamellar spacing in the Cu-Ag eutectic are compared with the results of Spitzig et al. for Cu-Nb alloys [94] and Embury et al. for pearlite [117] in Figure 14, where

$$\lambda/\lambda_0 = \exp(-0.36\eta) \text{ for Cu-Nb} \quad (4-3)$$

$$\lambda/\lambda_0 = \exp(-0.50\eta) \text{ for pearlite} \quad (4-4)$$

Although Spitzig et al. explained that the departure of the exponent from the ideal value (-0.5) is due to the increase in filament density at high deformation levels, the morphologies of the Nb filaments or the eutectic constituents could be partially responsible for this deviation. Combining equation (4-1) and (4-2) gives

$$\sigma = 297 + k(\lambda_0)^{-1/2} \exp(-0.20\eta) \quad (4-5)$$

This equation indicates that the strength of the DS 58 eutectic alloy is a function of both initial interlamellar spacing (λ_0) and draw ratio (η) and the reasonable fit with this equation is plotted in Figure 15 and 16. Therefore, the strength of the Cu-Ag alloys appears to follow the barrier model of strengthening mechanisms suggested by Embury et al. relatively well and shows similar behavior with the Cu-Nb alloys.

The variation of the UTS on η for the DS 10 and DS 58 alloys is shown in Figure 17. The UTS of the DS 58 alloy is about 300~350 MPa higher than that of the DS 10 alloy at a given η . Considering that the strengthening of in-situ microcomposites of this type is governed by the amount of interfacial area between the phases [6], it is concluded that the higher strength in the DS 58 alloy is due to its larger volume fraction of eutectic lamellae containing a larger amount of interphase interfaces.

For uniform deformation, the draw ratio $\eta = \ln(A_0/A)$ can be expressed as the true strain, $\ln(L/L_0)$, where L_0 and L are, respectively, the initial and instantaneous lengths of the wire specimens. Therefore, the slope, $d\sigma/d\eta$, of the σ vs. η plot is a measure of the hardening rate of the material. The higher strength of the DS 58 alloy is expected in view of its larger volume fraction of eutectic and the overall finer scale. This result suggests that the high interphase interfacial area in Cu-Ag alloys increases the initial strength of the composite yet does not significantly affect the hardening rate. One possible reason for this behavior is the crystallographic nature of the interface relationship, that is, the crystal structure of both copper and silver is FCC. Thus, it is conceivable that the interfaces between these structures do not block the movement of dislocations as effectively as in, for example, FCC-BCC materials such as Cu-Nb. This assumes, of course, that the properties of the neighboring FCC crystals are somewhat similar. Moreover, the lamellar eutectic structure normally has a cube-cube orientation relationship between the phases and the habit plane between the lamellae is $\{100\}$ [82]. This specific orientation relationship may provide lower resistance of the interface to the transfer of glide dislocations across it since the slip planes are parallel. This result suggests that, although

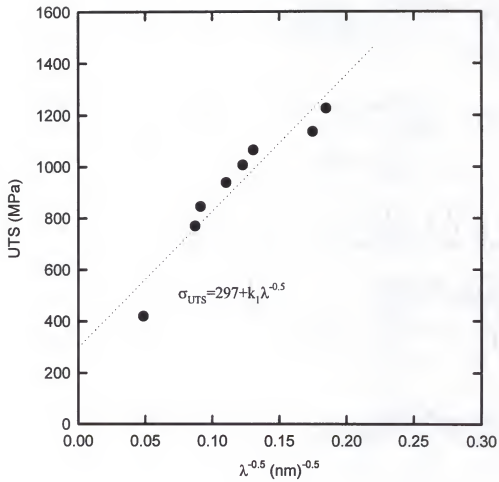


Figure 12. Variation of UTS on the interlamellar spacings (λ) of the DS 58 alloy.

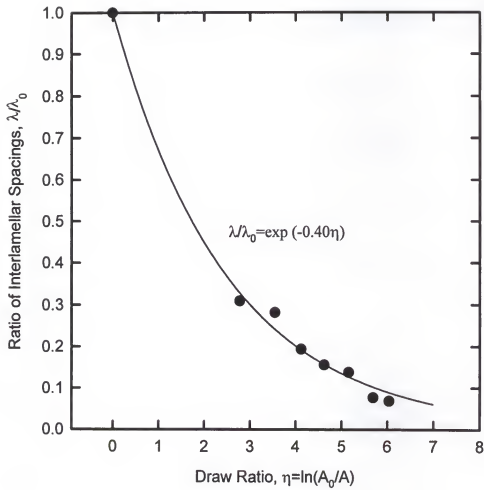


Figure 13. Variation of the ratio of interlamellar spacings (λ/λ_0) with draw ratio in the DS 58 alloy.

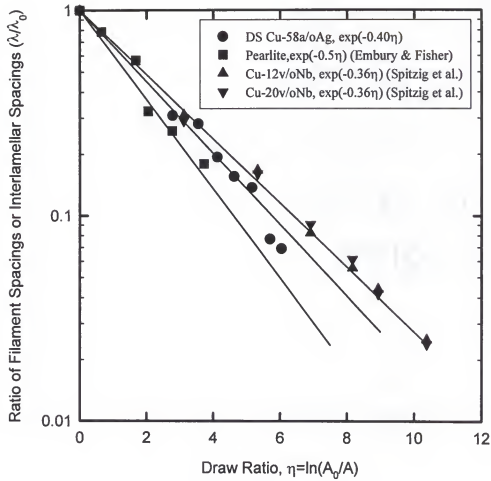


Figure 14. Variation in the ratio of interlamellar spacings (λ/λ_0) with draw ratio for the DS 58 and the Cu-Nb alloys.

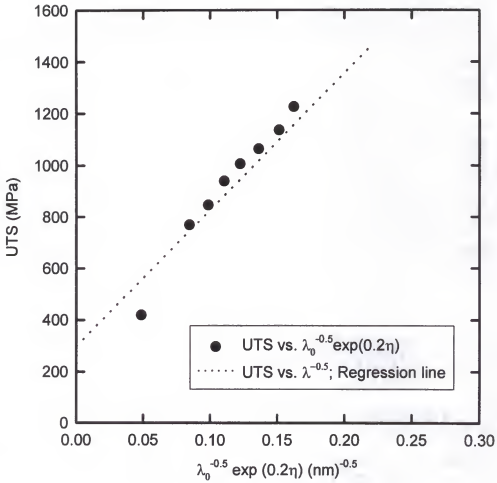


Figure 15. The dependence of UTS on the initial interlamellar spacing (λ_0) and draw ratio (η) of DS 58 alloy.

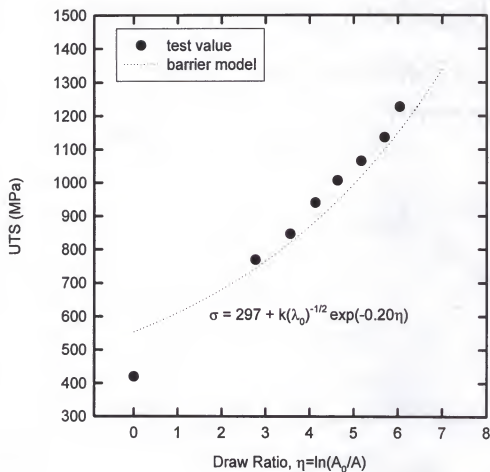


Figure 16. Comparison of the strength of the deformation-processed DS 58 alloy to the calculations based on the barrier strengthening model of strengthening mechanisms.

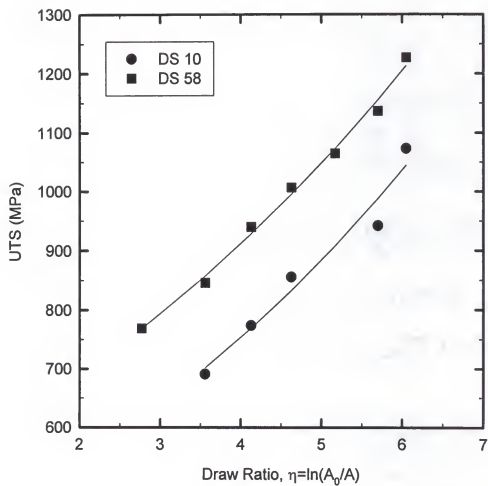


Figure 17. UTS dependence on the draw ratio for eutectic and off-eutectic alloys.

the interface contributes to the strengthening, the effect is not nearly as great as in the Cu-BCC alloys studied extensively.

4.1.3 Conductivity

Figure 18 shows that the conductivity of the eutectic alloy decreases more drastically than that of the off-eutectic (DS 10) alloy. Since the volume fraction of eutectic for the DS 10 alloy is approximately 11%, the completely eutectic DS 58 alloy contains a much higher amount of interfacial area. These interfaces act as scattering sources of free electrons and thereby reduce the mean free path of the electrons, causing the observed reduction in conductivity (two-dimensional size effect). The total resistivity of a composite, ρ_{tot} , can be expressed as

$$\rho_{tot} = \rho_t + \rho_d + \rho_b \quad (4-6)$$

where ρ_t is the resistivity increase due to thermal scattering, ρ_d the contribution due to lattice defects, and ρ_b the resistivity increase due to interphase boundaries. The estimated values of the mean free path are 43.0 nm for copper and 56.5 nm for silver at 293K [79]. Frommeyer et al. reported that there are anomalous decreases in conductivity when the fiber diameter becomes smaller than the mean free path of free electrons. For the DS 58 alloy with $\eta=2.8$, the estimated thickness of the copper lamellae is 35-40 nm and that of the silver is 95-100 nm. Because the size of the lamellae is close to the mean free path of the free electrons, the interface should become a more important scattering source as η increases. The conductivity of the DS 10 alloy containing ~11% of eutectic, however,

does not decrease as fast because the thickness of the dendrite is more than an order of magnitude larger than the interlamellar spacing. In this case, the overall magnitude of the interfacial area should be small. The reason for the lower conductivity of the DS 10 alloy at low deformation strains, where the interface effect is not as severe, is most likely due to the effect of the lower volume percent of silver, which has about 6% higher electrical conductivity than copper at 20°C [120]. In summary, at low draw ratios and relatively high interlamellar spacings, the volume fraction of silver is a dominant factor determining the total conductivity. However, with the increase in the deformation level, the amount of interfacial area becomes the more important factor especially when the interlamellar spacing gets close to the mean free path of the electrons in each phase.

4.1.4 Strength-Conductivity Factor

The strength and conductivity variations with draw ratio are replotted in terms of the strength dependence on the conductivity in Figure 19. While these plots show near-linear relationships, it is important to discuss the differences in slope and intercept in light of the ideas outlined above.

The slope of the strength vs. conductivity plot, $d\sigma/d\chi$, represents the relative sensitivity of the strength on the conductivity in these alloys. For convenience, let us define the strength-conductivity factor (SCF) as

$$\text{SCF} \equiv -d\sigma/d\chi \quad (4-7)$$

where σ is the UTS in MPa and χ the conductivity in %IACS. High SCF values imply

that it is possible to increase strength without sacrificing conductivity significantly; this is clearly the most desirable situation.

The dependence of strength on conductivity for both the DS 10 and DS 58 alloys is contrasted in Figure 19 where the data are compared to the regression line of the properties obtained by Sakai and coworkers for the TMP Cu-Ag alloys (Cu-8~32at%Ag) shown in Figure 4. Although the double heat treated (HT) TMP Cu-Ag alloys have a better combination of properties, the SCF values implies that the DS 10 alloy without TMP appears to have greater potential to provide greater strength at high deformation levels.

Figure 19 indicates that the DS 58 alloy has a lower SCF value than the DS 10 alloy. This suggests that the interphase interfaces have a larger influence on conductivity than on strength since the DS 58 alloy has a much higher volume fraction of eutectic. Therefore, it may be concluded that the interface strengthening may not be as effective for achieving high strength and high conductivity in Cu-Ag alloys as originally expected; as noted above, this is due to the detrimental effect of the interface on conductivity when the thickness of the lamellae becomes close to the mean free path of free electrons. A normalized UTS vs. conductivity plot is shown in Figure 20, where the slope of the plot was multiplied by the UTS at the corresponding conductivity. Clearly, the graph represents that the DS 10 alloy provides better combinations of strength and conductivity, because the DS 10 alloy has higher strength at all of the specific conductivity levels.

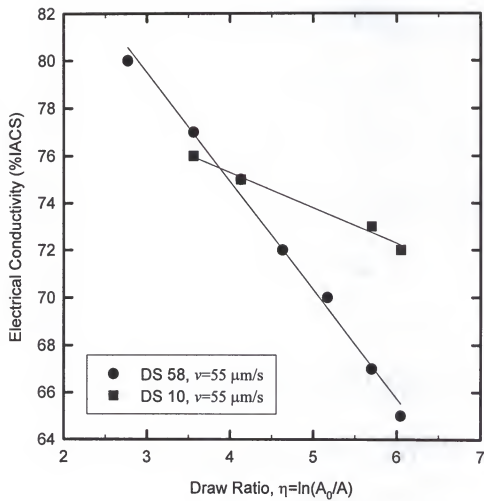


Figure 18. Electrical conductivity dependence on the draw ratio for eutectic and off-eutectic Cu-Ag alloys.

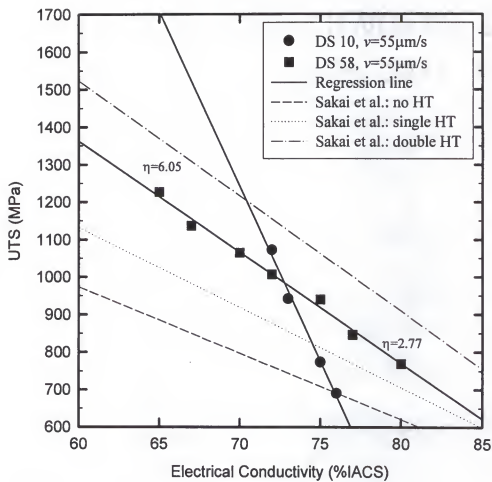


Figure 19. UTS dependence on the conductivity for eutectic and off-eutectic alloys.

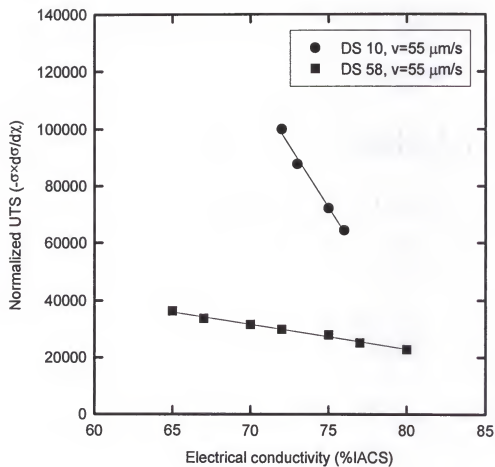


Figure 20. Normalized UTS dependence on the conductivity for eutectic and off-eutectic alloys.

4.2 Influence of Interlamellar Spacing

One of the merits of the directional solidification technique is that the withdrawal velocity, v , can be varied to produce a variety of interlamellar spacings, λ , according to [106]

$$\lambda^2 v = k G_L^{-r} \quad (4-8)$$

where k and r are constants and G_L is the temperature gradient in the liquid at the interface. Therefore, higher withdrawal speeds will cause smaller interlamellar spacings of the eutectic and these variations will effect both strength and conductivity.

In this study, comparisons were made between DS alloys grown at different rates and conventional mold cast alloys which have finer initial microstructures with little or no directionality.

4.2.1 Microstructures

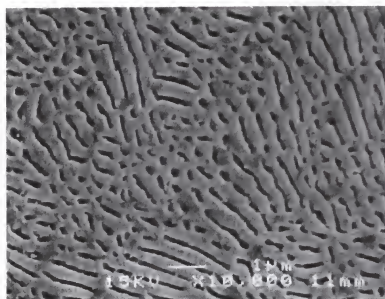
4.2.1.1 As-solidified structure

The SEM microstructures of the as-solidified eutectic (Cu-60a/oAg, DS 60) and near-eutectic (Cu-58a/oAg, DS 58) alloys obtained at different solidification rates are shown in Figure 21. The lamellar spacing of the eutectic alloy (DS 60) grown at the withdrawal speed of 2.5 $\mu\text{m}/\text{sec}$ (Figure 21 (a)) is of the order of 2.0~2.5 μm which is about four or five times larger than that for the DS 58 alloy grown at 55 $\mu\text{m}/\text{sec}$ (Figure 21 (b)). The conventionally-solidified chill cast Cu-58a/oAg (CS 58) alloy has much finer

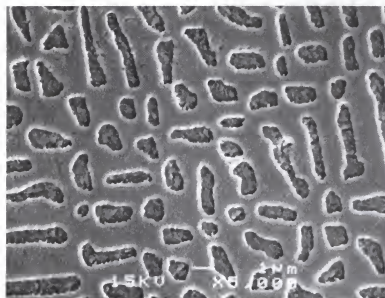
interlamellar spacing as shown in Figure 21 (c). These results indicate the strong dependence of lamellar spacing on solidification rate. The average interlamellar spacings of as-cast eutectic and near-eutectic alloys obtained at various withdrawal rates are listed in Table 4. In both alloys, it was noted that the minority copper phase tended to be less continuous in shape consistent with its volume fraction being near the boundary between lamellar and rod eutectics. The relative amount of “disconnection” of the copper lamellae is smaller in the DS 58 alloy than in the DS 60 alloy consistent with its slightly higher copper concentration/volume fraction.

4.1.1.2. As-deformed structures

The as-deformed microstructures of the DS 58 alloy after drawing to $\eta=2.8$ (corresponding to a reduction in area of 93.9%) are shown in Figure 22. As expected, the structures consist of fine lamellae of the copper and silver phases. The average interlamellar spacing, λ , is about 130~140 nm, with the width of the copper lamellae ~40 nm. These values are in agreement with the theoretical volume fraction of the Cu-rich phase for this composition indicating that there is negligible preferential deformation between the Cu-rich and Ag-rich phases. This behavior is considerably different from that found in Cu-X microcomposites (X=Nb, Ta, or Cr) where significant differential deformation occurs because of the large property differences between the constituent phases. In a similar manner, the CS Cu-58Ag ingot (Figure 23) displays a considerably finer interlamellar spacing of about 40 nm after deforming to $\eta\sim 3.1$; in this case, the average width of the minority copper phase is 10-15 nm.



(a)



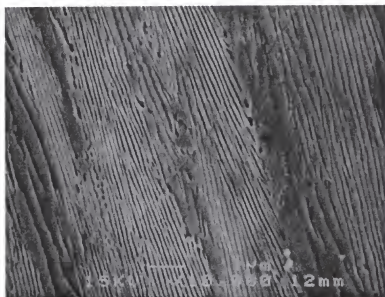
(b)

Figure 21. SEM microstructures of as-solidified ingots.

(a) DS 58 alloy, 55 $\mu\text{m}/\text{sec}$, transverse, etched

(b) DS 60 alloy, 2.5 $\mu\text{m}/\text{sec}$, transverse, etched

(c) CS 58 alloy, etched

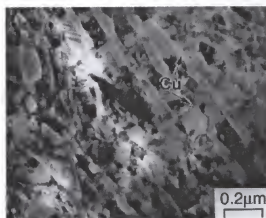


(c)

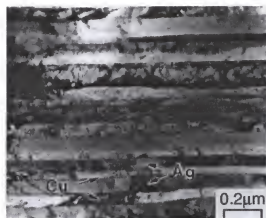
Figure 21--continued.

Table 4. Interlamellar spacings ($d_{Ag}+d_{Cu}$) of as-cast alloys for different withdrawal speeds.

Specimen ID	Withdrawal speed ($\mu\text{m}/\text{sec}$)	Average interlamellar spacing of as-cast specimens (nm)
DS 58	55	400~450
	12	780~1020
CS 58	-	140~200
DS 60	55	400~500
	2.5	2000~2500

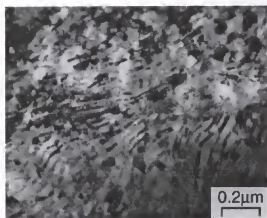


(a) Transverse

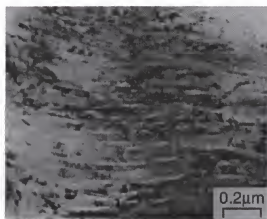


(b) Longitudinal

Figure 22. BF TEM of DS Cu-58Ag ($v=55 \mu\text{m}/\text{sec}$) after $\eta=2.8$.



(a) Transverse



(b) Longitudinal

Figure 23. BF TEM of CS Cu-58Ag after $\eta=3.1$.

The deformation characteristics of the CS 58 alloy are somewhat different from those of the DS material of the same composition. For the longitudinal section, the lamellae of the CS material exhibit a rather wavy shape while those of the DS alloy are relatively straight. The reason for this behavior in the CS materials is probably due to the re-orientation of neighboring colonies during deformation as shown schematically in Figure 24. The lamellae in the DS alloy, on the other hand, are already aligned parallel to the growth direction (Figure 22(b)) such that little re-orientation occurs during drawing. As seen in Figure 25 (a)-(d), the as-cast interlamellar spacing of 400~450 nm in the DS 58 alloy was reduced gradually by the deformation to ~30 nm at a $\eta=6.4$; again, the deformation ratio between the copper and silver phases was similar, as mentioned above.

4.2.2 Strength

The effects of withdrawal speed on the strength of DS 58 and DS 60 alloys after deformation are shown in Figure 26. The DS 60 alloy, with initial interlamellar spacing of 400~500 nm, corresponding to a withdrawal speed of 55 $\mu\text{m}/\text{sec}$ (Table 4), has tensile strengths that are approximately 180~200 MPa higher than the specimen of the same composition with larger interlamellar spacing obtained at $v=2.5 \mu\text{m}/\text{sec}$. Although there have been no quantitative measurements performed, the above observation suggests a Hall-Petch type of strengthening for the lamellar eutectic alloys. The alloys with larger interlamellar spacings tend to exhibit a little higher hardening rates although the strength levels are lower, consistent with the results for the Cu-20 %Nb alloy [69]. The strength of the alloy with the smaller interlamellar spacing at zero deformation is also expected to be higher. The conventionally-solidified ingot has about three times smaller interlamellar

spacing compared to the DS ingot of the same composition solidified at a withdrawal speed of 55 $\mu\text{m}/\text{sec}$ and a strength of about 200 MPa higher than that of the DS alloy at the same η value. The growth morphology of the eutectic could be another factor contributing to the strength of the alloys. As discussed in the previous section, the eutectic of the DS 58 alloy has a more lamellar morphology, giving higher UTS at the same deformation level compared to the DS 60 alloy; this morphological effect will be discussed in greater detail in section 4.4.

4.2.3 Conductivity

The electrical conductivity of the DS 60 eutectic structure with larger interlamellar spacing decreases more slowly (20-25%) with draw ratio than the DS 58 alloy (see Figure 27). The absolute value of the conductivity is also larger for the DS 60 alloy at all η values studied. Of the three contributing factors in Equation (4-6), the phonon scattering term, ρ_l can be assumed to be constant during room temperature testing. The lattice defects involved in the ρ_d term would be mostly dislocations. However, the density of dislocations in copper is known to saturate at a certain level ($10^{10} \sim 10^{11} \text{cm}^{-2}$) for heavily drawn wire because the FCC copper and silver undergo dynamic recovery during room temperature drawing. The tensile strength of pure silver tends to decrease with deformation above draw ratios of 4.5 [7]. Verhoeven et al. [11] have reported that the dislocation scattering contribution to the resistivity of a drawn Cu-Nb alloy is constant at η values above around 4. The defect scattering contribution, ρ_d , therefore, can be neglected. Thus, the main contributing factor to the resistivity increase in the specimen of smaller interlamellar spacing would be the interphase boundary

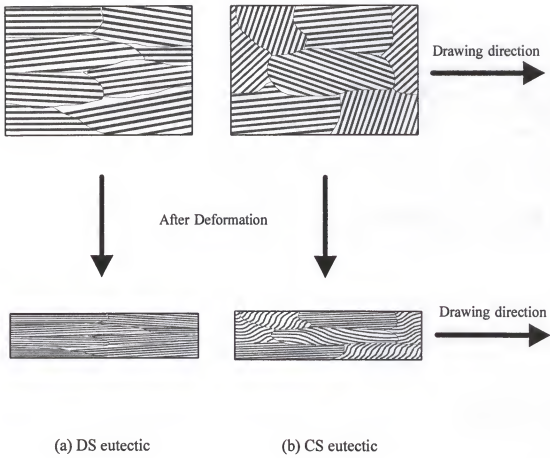


Figure 24. Schematic representing the differences in deformation behavior between the DS and CS alloys.

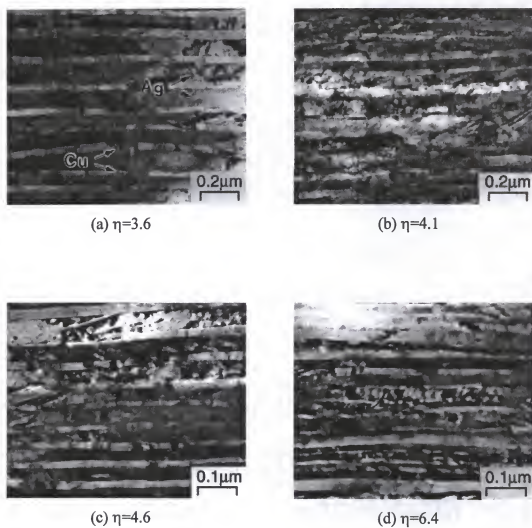


Figure 25. BF TEMs of the DS 58 alloy after different deformation levels.
(longitudinal, $v=55\text{ }\mu\text{m/sec}$)

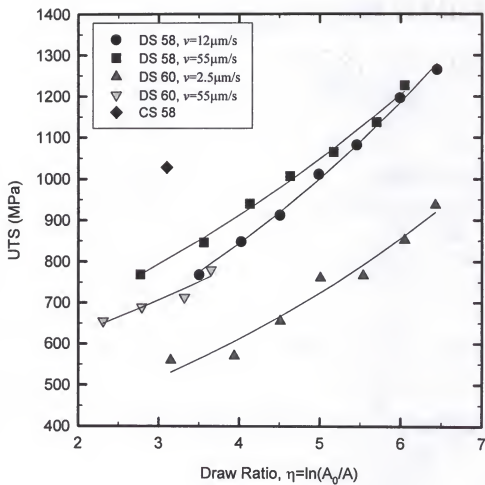


Figure 26. Dependence of UTS on withdrawal speed and draw ratio.

contribution, ρ_b . Specifically, if the thickness of the lamellae is decreased by four or five times, the interphase boundary density (amount of boundary/unit volume) for a given volume is increased by that ratio and causes a corresponding reduction in conductivity. Moreover, the interlamellar spacing of the DS 60 alloy at $\eta=2.8$ is well above the calculated mean free path for electron scattering; this is probably the reason for the lower slope of the conductivity-to-draw ratio plot.

As expected, the CS 58 alloy with the much finer interlamellar spacing, shows much lower conductivity than the DS 58 alloy at the same draw ratio. The electrical conductivity of the chill cast CS alloy is shown to be more sensitive to draw ratio than the DS 58 alloy; this is presumably because of its higher interfacial area and smaller interlamellar spacing. Therefore, the smaller the initial interlamellar spacing, the higher the sensitivity of conductivity on the draw ratio.

The y-axis intersection (conductivity) in Table 5 obtained by extrapolation of the Cu-60Ag eutectic alloy is in good agreement with the as-cast conductivity data of the same composition obtained by Frommeyer and Wassermann [79]. Their results also show that a conventionally-cast eutectic alloy has a conductivity of about 92% IACS which is lower than that of the DS 60 alloy, obviously due to the increased interphase interface density. Considering the fact that the DS 58 alloy contains slightly lower volume percentage of silver and was solidified at a slower rate than the CS alloy, this conductivity value for the DS 58 alloy is in reasonable agreement with the experimental data reported.

4.2.4 Strength-Conductivity Factor

The effect of withdrawal speed (interlamellar spacing) on the SCF values is given in Figure 28, where the regression lines of the data obtained by Sakai and coworkers are also indicated. For the conditions studied, the DS 58 alloy grown at $v=55\mu\text{m/sec}$ shows about three or four times larger interlamellar spacing than the DS 58 alloy grown at $v=12\mu\text{m/sec}$. The SCF value of the DS 58 alloy grown at the lower speed is about 25% higher than that of the DS 58 alloy grown at the higher speed, which has the lowest overall value in this study. Although this difference is not too high in view of the fact that the DS 10 alloy grown at the same speed shows more than 200% higher SCF than that of the DS 58 alloy, there should be a certain effect of interlamellar spacing on the SCF, that is, larger interlamellar spacings tend to have higher SCF values. Figure 28 indicates that at higher deformation ($\eta \sim 5$), the relative strength at a given conductivity is higher for the eutectic alloy (DS 58, $v=12$) with larger interlamellar spacing whereas, at lower deformation levels ($\eta < 4$), the relative strength is higher for the alloy with the smaller interlamellar spacing (DS 58, $v=55$).

These results indicate that, at higher deformation levels, the conductivity decrease due to the smaller λ (higher interfacial area) is higher than the strength increase due to the same. This is presumably related to the fact that the interlamellar spacings get closer to the mean free path of free electrons in both phases at the higher deformation levels. The other probable reason for this behavior is due to the relative strength increase resulting from the increased hardening rate for the alloy with larger interlamellar spacings. Specifically, since interphase boundaries can act as sinks for dislocations and since the density of sources should decrease with decreasing λ , the maximum dislocation density

that the material will develop should decrease with the increase in interface density (interfacial area/unit volume), assuming the same matrix properties. This could be a reason for the increased hardening rate in the alloy with larger interlamellar spacings. At lower deformation levels, however, the relative conductivity decrease due to interphase interfaces is not as effective as the relative strength increase by the interfaces because the interlamellar spacing is much larger than the mean free path of electrons in both phases. Also, the influence of the interfacial area on reducing the maximum dislocation density is not as effective. Therefore, the alloy with smaller interlamellar spacings can have higher relative strength in this case. In summary, the alloys with larger interlamellar spacings provide better combinations of strength and conductivity at the higher deformation levels. On the contrary, the alloys with smaller interlamellar spacings provide a better combination of properties at the lower deformation levels. Overall however, a eutectic alloy with large interlamellar spacing is preferred because of the lower sensitivity of conductivity to lamellar spacing and the higher hardening rate, which can be deduced from the normalized UTS-conductivity plot presented in Figure 29.

4.3 Influence of Initial Orientation of Lamellae

4.3.1 Microstructure

The microstructure of conventionally chill cast Cu-Ag eutectic alloys consists of randomly oriented lamellar colonies. Each colony with its unique orientation should influence the strength and conductivity of the casting in a different way. To investigate the influence of the lamellar orientation on the properties, sections from a DS eutectic

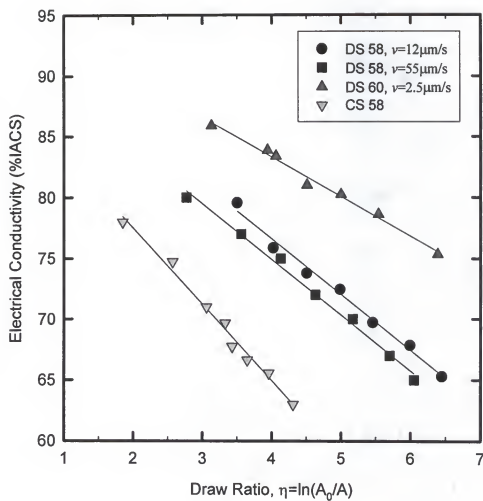


Figure 27. Electrical conductivity dependence on the withdrawal speed and draw ratio.

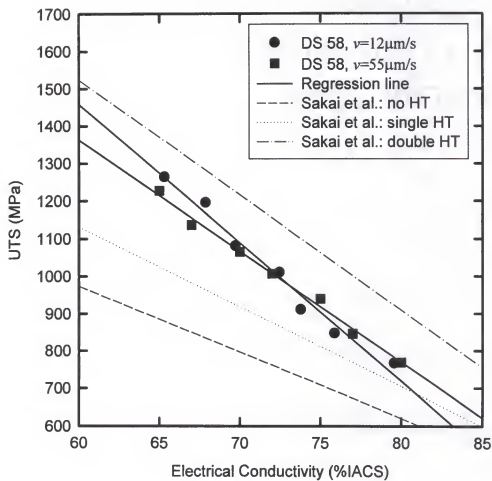


Figure 28. UTS dependence on the conductivity for eutectics with different interlamellar spacings.

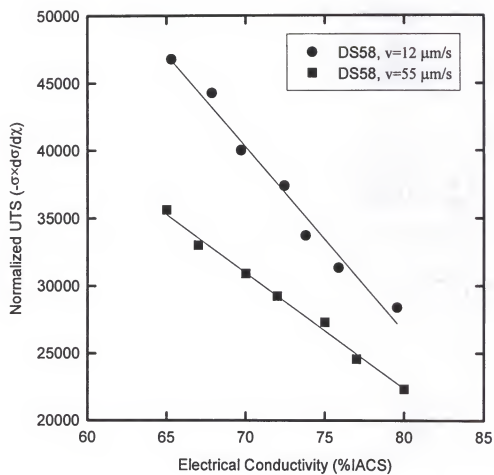


Figure 29. Normalized-UTS dependence on conductivity for eutectics with different interlamellar spacings.

Table 5. The slopes of the conductivity- η plots for various DS alloys.

Specimen ID No.	Withdrawal Speed ($\mu\text{m}/\text{sec}$)	Slope ($-\text{d}\chi/\text{d}\eta$)	y-axis intersection (%IACS)
DS 55	1.7	3.5	98.4
DS 58	55	4.6	93.3
	12	4.6	94.9
CS 58	-	6.5	91.0
DS 60	2.5	3.2	95.9
DS 65	1.7	3.4	97.2

ingot was cut 0° , 45° and 90° to the growth direction in order to study this effect.

By plotting UTS vs. η , the effect of initial lamellar orientation on the hardening rate ($d\sigma/d\eta$) can be determined. The conductivity vs. draw ratio plot provides the relative contribution of the initial lamellar orientation on the electrical conductivity of the Cu-Ag microcomposites. On the basis of these results, discussion was made on which orientation would be more useful in improving the combination of strength and conductivity. This is deduced by comparing the slopes of the strength vs. conductivity plots for the different initial lamellar orientations. The results were compared to the same specimen but processed by heat treatment in order to estimate the influence of precipitation on the orientation differences.

Figure 30 shows the transverse section of the DS Cu-58at%Ag alloy grown at a withdrawal speed of $12 \mu\text{m/sec}$. The longitudinal section of this alloy shows a microstructure in which lamellae of each phase are aligned parallel to the growth axis, as described in the previous section.

The microstructures of deformation-processed specimens are shown in Figure 31 and 32. The hydrostatic stress applied to the 90° orientation alloy (specimen perpendicular to the growth direction) results in wavy shape of the colony as shown in Figure 31 (a). The copper lamellae inside the colony exhibit relatively regularly-aligned deformation contours with a kinked deformation appearance as indicated in Figure 31 (b). This kinked nature of the lamellae suggests that the lamellar refinement should not occur as effectively as in the 0° -orientation alloy (specimen parallel to the growth direction) at low η values. Macroscopic deformation contours of the wires are contrasted in Figure 32. It is evident that the metal flow inside the wire during deformation occurs spirally.

However, the deformation contour in the 90° specimen is not as symmetrical as that in the 0°-orientation alloy. The reason is believed to be due to the directionality of the original ingots.

4.3.2 Strength

The strength vs. draw ratio of the DS Cu 58Ag alloy for the three different orientations is shown in Figure 33. The results indicate that there are no significant differences in hardening rates for the three specimens, although the 0° orientation specimens had the highest strength level at all the deformation ranges used in this study. In other words, the hardening rate does not appear to be a function of orientation ($d\sigma/d\eta \neq f(\phi)$) as originally suspected. The reason for the high strength for the 0° specimens is related to its relatively finer microstructure obtained during deformation, because this alloy should have less kinked area than the 90° specimens.

4.3.3 Conductivity

In contrast to the strength vs. orientation results, the conductivity drop with draw ratio was the highest for the 0° orientation (Figure 34). This is presumably due to the faster reduction in the interlamellar spacing for that orientation. In this case, the conductivity sensitivity on draw ratio ($d\chi/d\eta$) has the following order:

$$|d\chi/d\eta|_{0^\circ} > |d\chi/d\eta|_{45^\circ} > |d\chi/d\eta|_{90^\circ} \quad (4-9)$$

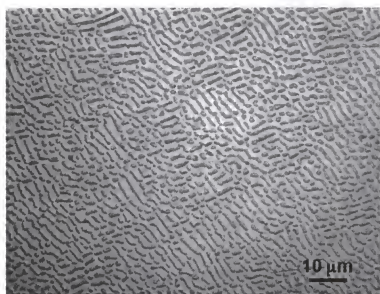
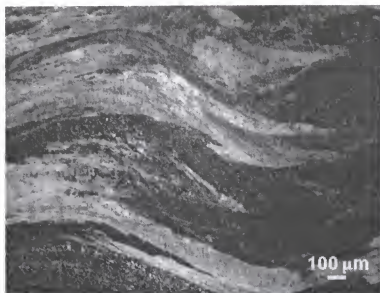
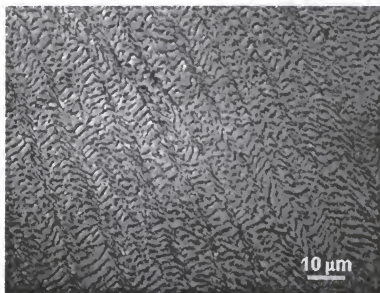


Figure 30. Optical microstructure of the DS 58 alloy.
(transverse, $v=12\text{ }\mu\text{m/sec}$, etched)

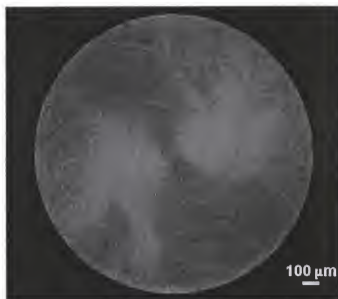


(a)

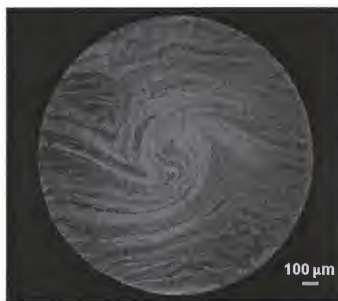


(b)

Figure 31. Deformation contour generated in the 90°-orientation alloy after 51%RA.
(a) Macro-deformation structure, transverse
(b) Micro-deformation structure, transverse



(a)



(b)

Figure 32. Macro deformation contour generated in the DS 58 alloy after 83%RA.
(a) 0°-orientation alloy; (b) 90°-orientation alloy

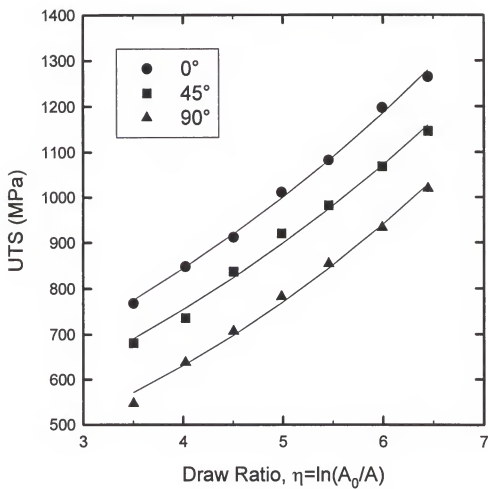


Figure 33. UTS dependence on draw ratio for alloys of different initial lamellar misorientations.

The fact that the conductivity sensitivity on draw ratio is a function of misorientation ($d\chi/d\eta=f(\phi)$) can be readily anticipated from the microstructural investigation. Figure 35 shows that the sensitivity of electrical conductivity to deformation decreases linearly as the initial misorientation increases from 0° with the highest conductivity levels occurring for the 90° -orientation alloy.

4.3.4 Combination of Strength and Conductivity

By combining these results, it is clear that the highest strength-conductivity factor (SCF) occurs in the specimens with lamellar orientations perpendicular to the growth axis (Figure 36 through 38). From the UTS-conductivity plot in Figure 36 and 37, we can deduce that the strength sensitivity on electrical conductivity (SCF) depends on the misorientation (linear function of misorientation) and is highest when the misorientation becomes maximum as shown in Figure 38. More quantitatively,

$$|d\sigma/d\chi|_{0^\circ} > |d\sigma/d\chi|_{45^\circ} > |d\sigma/d\chi|_{90^\circ} \quad (4-10)$$

When compared to the SCF results of Sakai and coworkers, the 90° -orientation specimen appears to have greater potential to provide greater strength at high deformation level. From the results of this study, it can be expected that the alloys with randomly-oriented lamellae should have better combinations of the strength and conductivity than directionally solidified alloys assuming the same interlamellar spacing. Therefore, conventional chill casting may be a better approach in order to improve the strength-conductivity combination in Cu-Ag eutectic alloy.

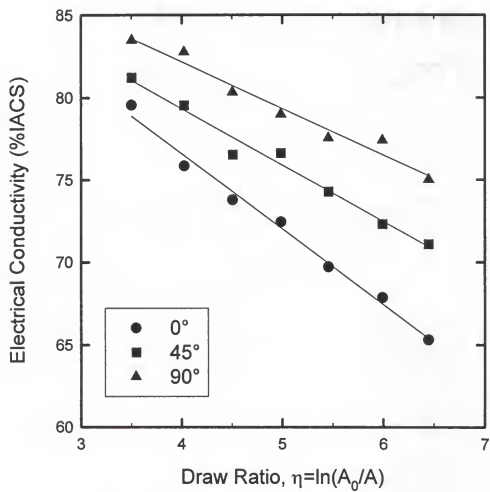


Figure 34. Electrical conductivity dependence on draw ratio for alloys of different initial lamellar misorientations.

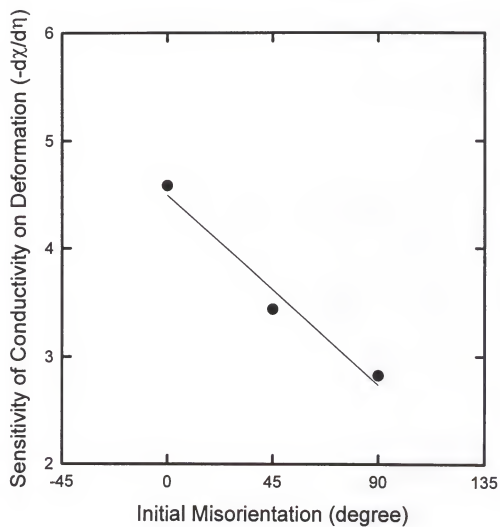


Figure 35. The variation of the deformation sensitivity of electrical conductivity on the initial misorientation.

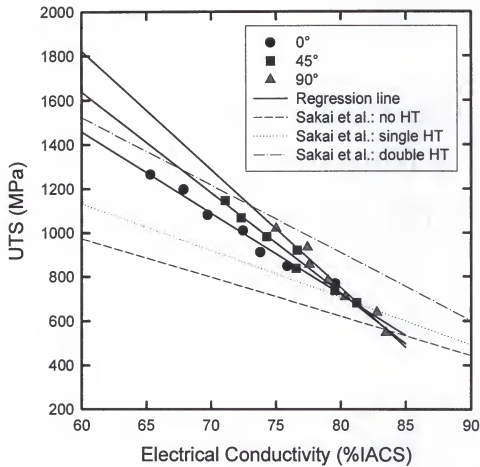


Figure 36. UTS dependence on electrical conductivity for alloys of different initial lamellar misorientations.

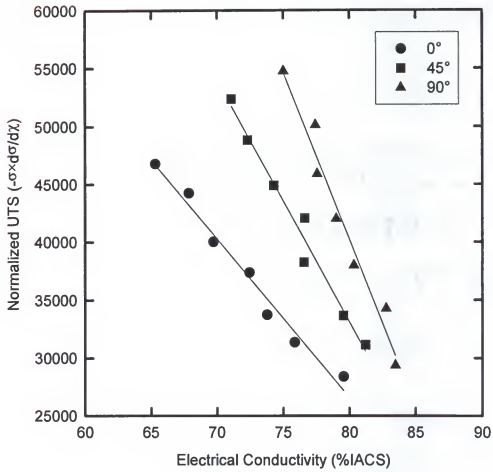


Figure 37. Normalized UTS vs. electrical conductivity for alloys of different initial lamellar misorientations.

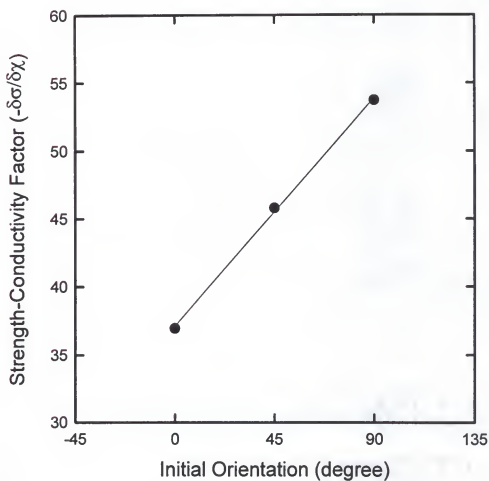


Figure 38. SCF showing UTS sensitivity on electrical conductivity and its variation on the initial lamellar misorientations.

4.3.5 Other Considerations

The sensitivity of both strength and electrical conductivity to the initial misorientation is shown in Figure 39 and 40 at different deformation levels. Clearly, the strength decreased with increasing initial misorientation at all η values. However, the sensitivity of the strength to the initial misorientation is roughly constant (Figure 39), while the sensitivity of conductivity depends on the amount of deformation (Figure 40). Figure 41 contrasts the rate of change in the sensitivity of strength ($d\sigma/d\phi$) and conductivity ($d\chi/d\phi$) on the initial misorientation. Both data are normalized by the strength and conductivity at $\eta=3.5$. Clearly, the alloy has little change in UTS sensitivity on misorientation at higher η values whereas the electrical conductivity increases by about 150% at $\eta=6.5$. The increased sensitivity of conductivity on misorientation at high deformation levels indicates that the reduced interlamellar spacing is a critical factor reducing the electrical conductivity, which is consistent with the results described in the previous sections.

4.4 Influence of Growth Morphology of Interdendritic Eutectic

The growth morphology of the eutectic influences both the strength and conductivity of the alloys. Theoretically, if the volume fraction of one phase is greater than $\sim 1/10$ and less than 0.28 or $1/\pi$ in a binary isotropic system, a rod-type eutectic morphology is predicted [121, 122]. Since the eutectic composition (Cu-60.2a/oAg) contains ~ 26 vol% of the copper phase whereas volume fractions greater than $0.28 \sim 1/\pi$ tend to favor a lamellar structure, it was of interest to grow slightly off-eutectic alloys so

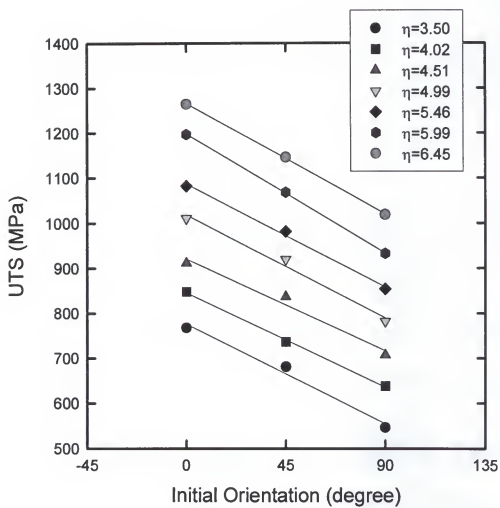


Figure 39. UTS sensitivity on the initial lamellar misorientations at various deformation levels.

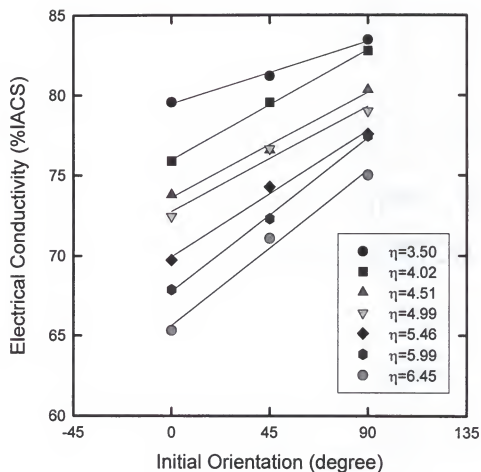


Figure 40. UTS sensitivity on the initial lamellar misorientations at various deformation levels.

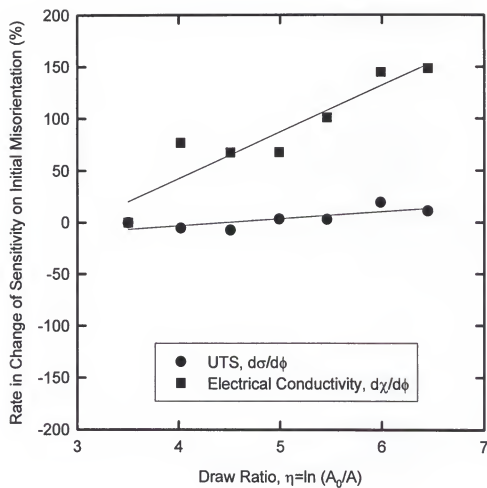


Figure 41. Rate in change of the sensitivity of strength and conductivity on initial misorientation at various deformation levels; the data are normalized by the properties at $\eta=3.5$.

as to produce either copper rods or copper lamellae in order to determine how the starting microstructure influences the properties that are produced during subsequent TMP. The purpose of this paper section was to evaluate the effect of the growth morphology of the initial interdendritic eutectic on both the strength and conductivity of these alloys as a function of TMP. The effect of the morphology on the deformation characteristics is also discussed.

For this purpose, both a hypoeutectic and a hypereutectic alloy were investigated. Comparison was made in terms of deformation characteristics, hardening rate, interlamellar spacing, and stress sensitivity on conductivity.

4.4.1 Microstructures

4.4.1.1 As-solidified structures

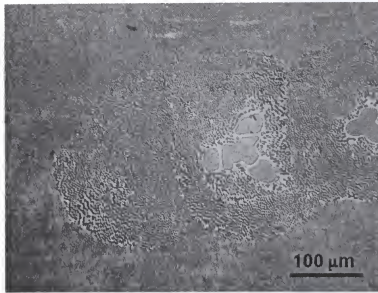
For steady-state coupled growth of off-eutectic alloys, high thermal gradients, G_L , and low growth velocities, v , are required according to the equation [106]:

$$G_L/v \geq -m_L(C_E - C)/D_L \quad (2-2)$$

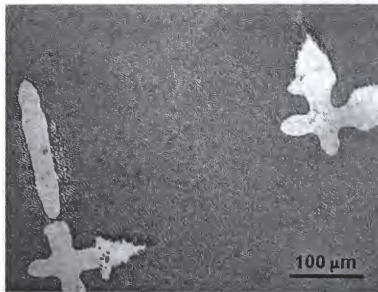
where m_L is the liquidus slope, C_E and C the eutectic and alloy compositions, respectively, and D_L the diffusivity in the liquid. Thus, it is clear that compositions near the eutectic can be grown in a coupled fashion at reasonable rates whereas the maximum velocity for growth of off-eutectic compositions may be prohibitively slow. Because the eutectic composition of this Cu-Ag system lies at the boundary expected for the lamellar to rod transition, the microstructures of the Cu-55at%Ag (DS 55) and Cu-65at%Ag (DS

65) alloys grown via coupled growth were expected to display lamellar and rod eutectics, respectively. However, the microstructures of the DS 55 and the DS 65 alloys grown at $1.7 \mu\text{m/sec}$ contained some primary dendrites as shown in Figure 42 and 43. This means that coupled growth does not occur in both alloys at the given experimental condition. According to the above equation, it becomes more difficult to grow off-eutectic alloys in a coupled fashion as the composition becomes further removed from the eutectic. For an alloy of a given composition, the main experimental variables are (1) temperature gradient in the liquid at the interface and (2) the withdrawal rate (interface velocity). The temperature gradient in the liquid is dependent upon the thermal conductivity of the material and decreases with increasing conductivity. Since both copper and silver have high thermal conductivities, it becomes difficult to obtain high temperature gradients at the solid/liquid interface. For reasonable growth rates, this limits the coupled growth of off-eutectic alloys to a narrow composition range near the eutectic composition.

The growth morphologies of the interdendritic eutectic near the primary phases in the DS 55 and DS 65 alloys are shown in Figure 44. Basically, the interdendritic eutectic around primary copper in the DS 55 alloy is rod-like while that around primary silver in the DS 65 alloy is more lamellar. These variations in structure are probably caused by the shift in the eutectic composition due to the differences in the compositions of the interdendritic liquid after development of the primary phases. Specifically, as the hypoeutectic DS 55 alloy is cooled from above the liquidus temperature, primary copper dendrites will form; during further cooling, the interdendritic liquid will be supercooled below T_E because of solute redistribution and capillarity effects. As such, the liquid will become silver-rich and solidify as a rod-like eutectic. When the nucleation of eutectic

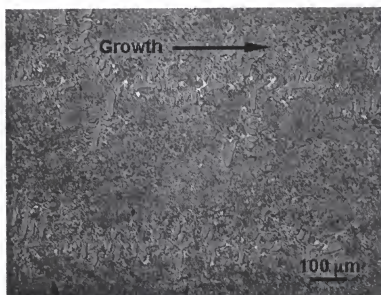


(a) DS 55

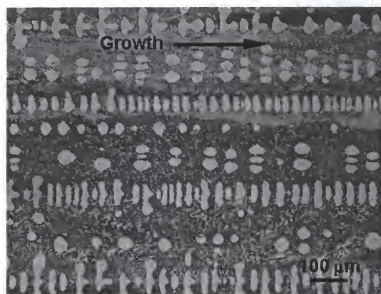


(b) DS 65

Figure 42. Optical microstructure of the DS 55 and DS 65 alloy showing primary phase and interdendritic eutectic (transverse, etched).
(a) DS 55; (b) DS 65

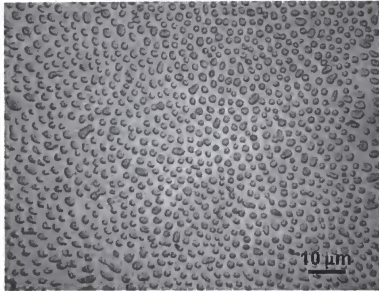


(a) DS 55

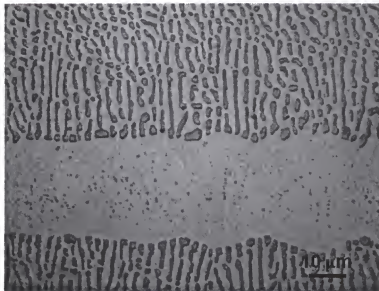


(b) DS 65

Figure 43. Optical microstructure of the DS 55 and DS 65 alloy showing growth nature of primary phases and interdendritic eutectic (longitudinal, etched).



(a) DS 55, rod



(b) DS 65, lamellae

Figure 44. Optical microstructure of the DS 55 and DS 65 alloy showing growth morphology of interdendritic eutectic adjacent to the primary phase (transverse, etched).

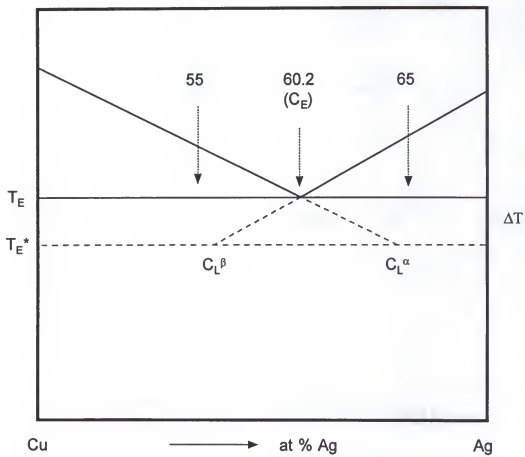


Figure 45. A schematic diagram showing the effect of undercooling below T_E on the composition of the interdendritic liquid prior to the eutectic formation in the presence of primary α -Cu or β -Ag.

phases occurs at a certain temperature, T_E^* , the average composition of the interdendritic liquid will be C_L^α (Figure 45). Because the eutectic composition of the Cu-Ag alloy is near the boundary of the rod to lamellar transition, this increased solute in the interdendritic liquid should favor the formation of a rod eutectic. For the same reason, the composition of the interdendritic liquid in the hypereutectic Cu-65a/oAg alloy will shift to the copper-rich side (to C_L^β) and thereby promote the formation of a lamellar eutectic structure. This shift in the interdendritic liquid composition is basically due to the presence of the primary phases and thus will be limited to the liquid immediately surrounding the primary phases.

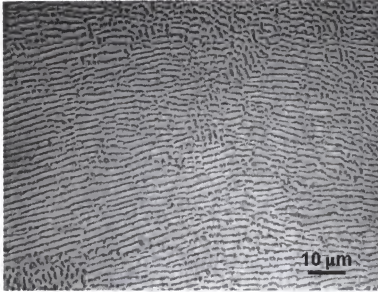
The growth morphologies of the interdendritic eutectic far away from the primary phases of the DS 55 and DS 65 alloys are shown in Figure 46 (a) and (b). The eutectic morphology of the DS 55 alloy in Figure 46 (a) appears to be more lamellar than that of the DS 65 alloy which tends towards a rod eutectic. These differences in morphology are considered to be the result of localized coupled growth of the interdendritic eutectic under the imposed experimental conditions. Although the compositional deviations from the equilibrium eutectic are only 2-3 % in volume fraction, this value is enough to change the eutectic morphology because the equilibrium eutectic composition of Cu-Ag system is close to the boundary of the rod-lamellar transition. Bluni and coworkers [122] calculated when the volume fraction of minor phase in a eutectic is lower than 0.28, the surface energy per interphase spacing becomes lower at rod eutectic, leading to the formation of rod eutectic (Figure 47). In the Cu-Ag system, the volume fraction of the copper phase in the eutectic is 0.26 at the eutectic temperature, 779 °C. The 2-3 % deviation in volume fraction to the copper-rich side results in an increase in the volume fraction of the copper

to 0.28-0.29; this may result in a morphological change to a more lamellar structure. The average aspect ratio (length-to-width ratio) of the interdendritic eutectic far away from the primary phases in the DS 55 alloy is about 70% to 105% higher than that in the DS 65 alloy which means that the eutectic in the DS 55 alloy is more lamellar-like ("lamellar") than that in the DS 65 alloy which is more rod-like ("rod").

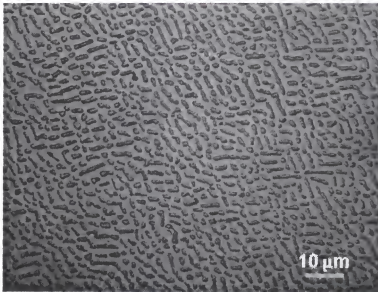
Since the rod eutectic in the DS 55 alloy is limited to the regions adjacent to the primary copper and the volume fraction of eutectic is about 92 vol%, most of the mechanical and physical properties of the DS 55 alloy should be dominated by the lamellar eutectic. In the same way, the rod eutectic in the DS 65 alloy will govern the mechanical and physical properties. Therefore, the properties of these materials may be dominated by the nature of the eutectic constituent.

4.4.1.2 As-deformed structures

The microstructures (transverse to the deformation axis) of the interdendritic eutectic regions in the deformation-processed DS 55 and DS 65 alloy wires, are shown in Figures 48 and 49, respectively, at several different draw ratios. Figure 48 (a) represents the deformed rod eutectic around the primary copper. Because of the hydrostatic nature of the applied stress, the copper rod aligned to parallel to deformation axis does not much elongated to the transverse direction of the wire. Some fragmentation of the copper phase was observed in both specimens partly due to the axially symmetric deformation process. However, the distribution of the fragmented copper fibers is not as regular as the fibrous microstructure obtained in the eutectic alloy at $\eta \approx 6.9$ by Frommeyer and Schneider [107].



(a) DS 55, lamellar-like



(b) DS 65, rod-like

Figure 46. Optical microstructure of the DS 55 and DS 65 alloy showing growth morphololgy of interdendritic eutectic far away from primary phases (transverse, etched).

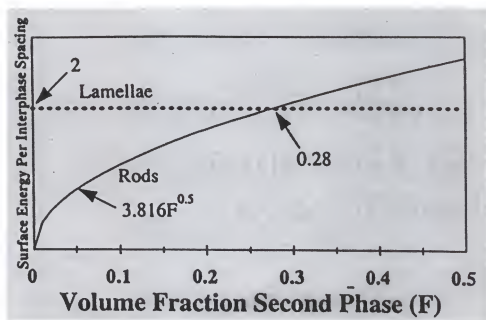


Figure 47. Surface energy produced by rod and lamellar eutectic growth as a function of volume fraction of second phase [122].

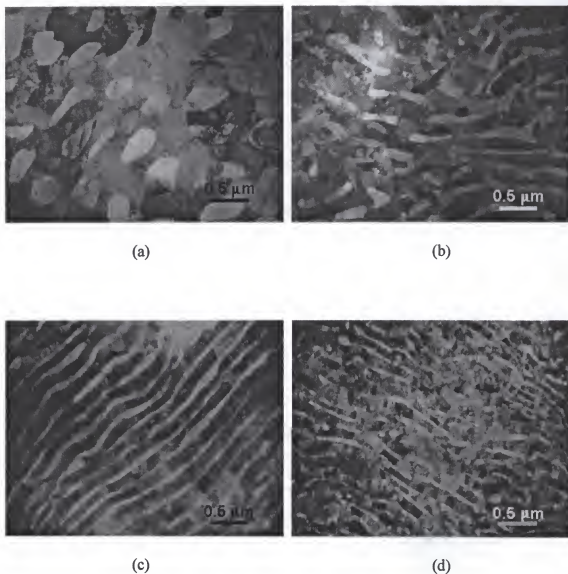


Figure 48. BFTEMs of transverse sections of the DS 55 alloy at various deformation levels.

- (a) rod eutectic around primary phase at $\eta=3.56$
- (b) lamellar-like eutectic away from the eutectic at $\eta=3.56$
- (c) lamellar-like eutectic away from the eutectic at $\eta=5.17$
- (d) lamellar-like eutectic away from the eutectic at $\eta=6.05$

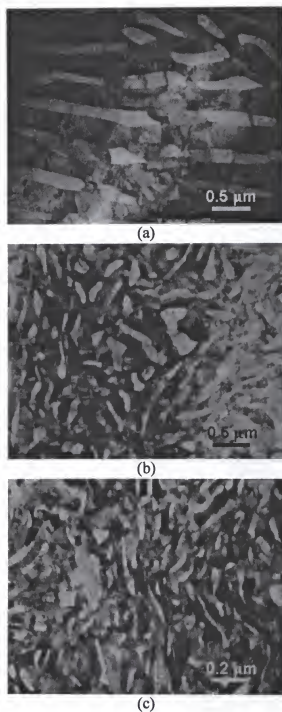


Figure 49. BFTEMs of transverse sections of the DS 65 alloy after various deformation levels.

- (a) rod-like eutectic away from the eutectic at $\eta=3.56$
- (b) rod-like eutectic away from the eutectic at $\eta=5.17$
- (c) rod-like eutectic away from the eutectic at $\eta=6.05$

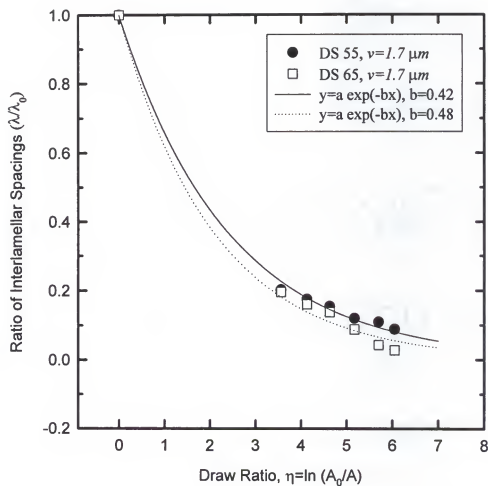


Figure 50. Comparison of the reduction rate in interlamellar spacings for the alloys with different eutectic morphologies.

Apparently, the copper phases in the DS 55 alloy appear more lamellar in nature than that in the DS 65 alloy. The deformation-induced fragmentation proposed by Frommeyer and Schneider does not occur so severely even at $\eta=6.05$. Rather, both alloys maintain their morphologies, although some partially kinked regions are observed. The relatively small aspect ratio of the copper phase observed in the DS 65 alloy appears to have resulted from the morphological variation produced upon solidification.

Surprisingly remarkable differences in both the size (thickness) of both phases and in their resultant interlamellar spacings were observed in these two alloys. The diameter/thickness ratio of the copper phase in the DS 55 alloy is much larger than that of the DS 65 alloy at $\eta=6.05$ although the thickness of each phase was higher in the DS 65 alloy in the as-cast condition. The variation of the interlamellar spacings on draw ratio for both alloys is shown in Figure 50 where the interlamellar spacings is normalized by the initial values (λ_0) of each alloy. And it is apparent that the interlamellar spacings of the DS 65 alloy are reduced faster than those of the DS 55 alloy. The reason for the higher reduction rate in the eutectic spacing is due to the hydrostatic nature of the applied stress combined with the rod-like morphology. The hydrostatic stress will enhance for the copper "rod" to get closer each other while it produce kinks in the lamellar-like eutectic for the DS 55 alloys. The interlamellar spacings at $\eta=6.05$ is about 110-170 nm for the DS 55 alloy and 50-80 nm for the DS 65 alloy.

4.4.2 Strength and Conductivity of DS alloys

4.4.2.1 Strength

A plot of UTS vs. draw ratio (Figure 51) indicates that the DS 65 alloy hardens more rapidly than the DS 55 alloy even though the UTS of the latter is higher at low η values. There are various possible reasons for this difference in hardening rate including (1) the differences in the nature (species and volume fraction) of the primary phases, (2) the different morphologies of the interdendritic eutectics (lamellae vs. rods) and (3) the different responses of the eutectic to deformation.

In an effort to elucidate which mechanism(s) is responsible for the observed behavior, the microhardness of the primary phase in the as-solidified ingots were measured. As expected, the hardness of the copper-rich primary phase was higher than that of the silver-rich phase (82 vs. 67 kg/mm²) in spite of the higher solubility of copper in silver than silver in copper (14.1 a/o vs. 4.9 a/o at the eutectic temperature). It should be mentioned that the work hardening rate of pure copper is greater than that of pure silver [7] suggesting that the copper phase is harder at all η values. This implies that the primary phase is not responsible for the observed behavior.

Since the volume fraction of eutectic is greater in the DS 55 alloy, based on simple lever rule considerations, it is not surprising that the copper-rich alloy is harder at the low η values. As the deformation increases, however, the overall strength becomes higher for the DS 65 alloy at $\eta > 5$ since the scale of the rod structure decreases more rapidly during deformation. Therefore, the reason for the higher strength at high deformation level for the DS 65 alloy is due to the “morphology-induced” fine microstructural scale.

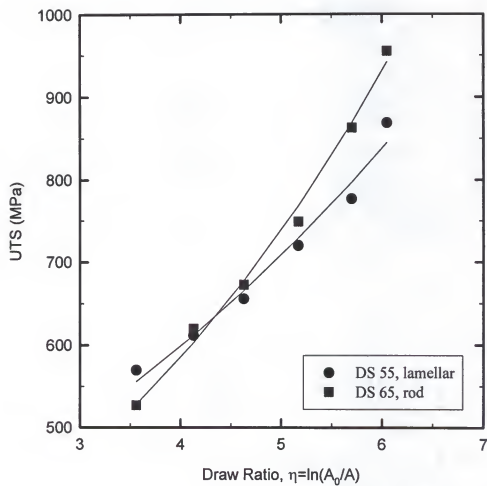


Figure 51. UTS dependence on draw ratio (η) for the alloys with different eutectic morphology.

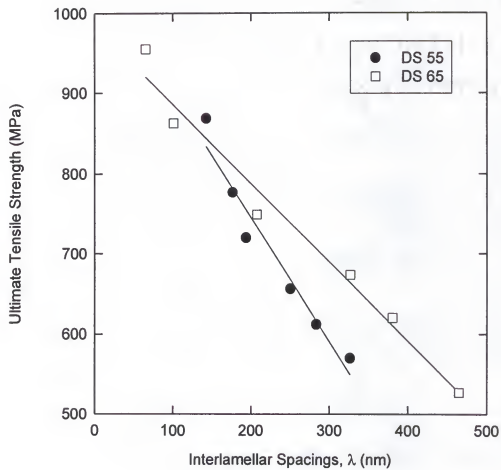


Figure 52. UTS dependence on interlamellar spacings for the alloys with different eutectic morphology.

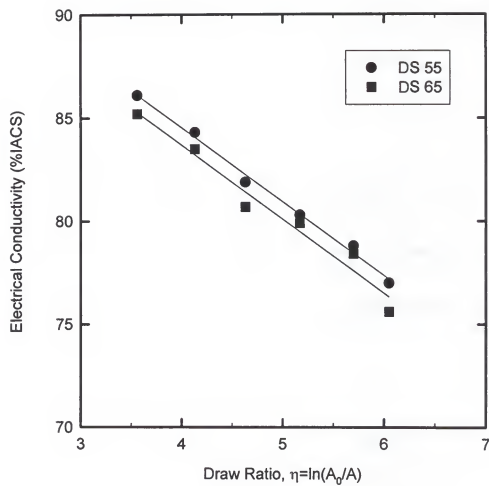


Figure 53. Electrical conductivity dependence on draw ratio for the alloys with different eutectic morphologies.

In order to investigate the influence of each eutectic morphology on the strength, the UTS is plotted in terms of the interlamellar spacing, λ , in Figure 52. The lamellar eutectic in the DS 55 alloy provides higher strengthening for a given reduction in λ , which is consistent with the predictions by Kuhlmann-Wilsdorf [123]. These results indicate that the lamellar structures are preferable from a work hardening standpoint and that the composition and solidification methods are important for selecting the appropriate structure. Furthermore, the strength contribution of the lamellar eutectic is greater at low interlamellar spacings.

4.4.2.2 Conductivity

Figure 53 shows that the DS 55 alloy has a little higher conductivity than the DS 65 alloy at all strain levels. As mentioned above, the volume fraction of primary phase in the DS 55 alloy is about 2.5 times lower than that for the DS 65 alloy and the electrical conductivity of the primary copper is expected to be lower than that of the primary silver. Moreover, the total volume fraction of silver is also lower in the DS 55 alloy. In order to explain the higher conductivity for the DS 55 alloy, the following three factors should be considered. The first factor is the effect of the primary phases on conductivity. The room temperature solid solubility of silver in copper is almost negligible (<0.06 at%Ag at 200°C) while that of copper in silver is about 0.3 at%Cu [100]. In general, solute atoms in silver decrease its conductivity drastically depending on the particular species. As expected, copper is not as potent as many other elements in reducing the conductivity of silver [124]. Considering the fact that the room temperature resistivity of silver is a linear function of copper concentration with a slope of $0.1 \mu\Omega\text{-cm/at\%Cu}$ [125], the

conductivity drop of silver due to the solute copper is about 1.9 %IACS [120]. This means that the primary silver phase still has higher conductivity than primary copper. With the slow growth rate of 1.7 $\mu\text{m/s}$ in these alloys, it can be assumed that any excess solute atoms dissolved in the silver matrix should have an almost negligible effect. Therefore, it seems unlikely that the increased volume fraction of the primary silver phase (containing copper) causes the lower conductivity in the DS 65 alloy. Rather, the primary silver should increase the conductivity of the DS 65 alloy if everything else is equal.

The second factor to be considered is the influence of the interdendritic eutectics. Because the DS 65 alloy has much finer interdendritic eutectic at high deformation strains, the interdendritic eutectic constituent may become the dominant factor at higher deformation levels ($\eta > \sim 5$). The fine scale eutectic in the DS 65 alloy reduces the conductivity more effectively, resulting in the lower conductivity at high strain.

The other possible reason for the conductivity differences is the morphological effects of the eutectic phases. Because the DS 55 and DS 65 alloys contain, respectively, $\sim 92\%$ and $\sim 80\%$ of the eutectic, most of the properties are expected to be effected by the nature of the eutectics. From the microstructural comparison in Figures 48 and 49, it is evident that the DS 65 alloy has a coarser structure than the DS 55 alloy at low deformation levels. Therefore, higher conductivity may be expected in the DS 65 alloy at low deformations. The conductivity of the DS 55 alloy, however, is higher than that of the DS 65 alloy at all strains. Therefore, the reason for the higher conductivity of the DS 55 alloy must result from the morphological differences of the interdendritic eutectic.

Figure 54 represents the variation of electrical conductivity on interlamellar spacings. The conductivity of the DS 55 alloy with the lamellar eutectic decreases more

rapidly than that of the DS 65 alloy with the rod eutectic. In other words, the DS 55 alloy exhibits a higher sensitivity of electrical conductivity on interlamellar spacing, λ . This figure also indicates that the lamellar eutectic greatly reduces electrical conductivity especially when interlamellar spacings approach the mean free path of electrons in the constituent phases (43 and 56.5 nm at room temperature for Cu and Ag, respectively [79]); this is consistent with the results of Frommeyer and Wassermann [79]. In addition, the lamellar eutectic provides higher conductivity at large interlamellar spacings (low deformation levels) presumably due to the lower interphase interfacial area generated by deformation. This morphological effect is believed to be the major factor for the higher conductivity of the DS 55 alloy at low strains.

Therefore, it can be concluded that the main reason for the higher conductivity of the DS 55 alloy at all η values is due to the effect of the morphological differences in the eutectic phases involved and their different responses to deformation processing. This morphological effect is thought to be a major factor lowering the electrical conductivity of the DS 65 alloy at low deformation levels. Combined with the behavior at high deformation levels, it is clear that the morphological effect lowers the overall conductivity of the DS 65 alloy.

Because of the combined effects between the size and morphological variation of the interdendritic eutectic, the slope of the χ vs. η plot in Figure 53 is similar in both the DS 55 and DS 65 alloys. However, if it is assumed that there are no differences in the interlamellar spacing of the interdendritic eutectics, the morphological variation should influence the slope of the χ vs. η plot. The sensitivity of the conductivity to deformation, therefore, is effected by the amount of the eutectic, the volume fraction of silver, the

interlamellar spacing, and the morphological variations of the eutectic.

4.4.2.3 Strength and conductivity

When describing high strength, high conductivity alloys, it is common to plot strength vs. conductivity for comparative purposes. When this is done for the two off-eutectic alloys (Figure 55), it is clear that the DS 55 alloy has superior properties at low deformation levels (low strength, high conductivity regime) and inferior properties at the higher deformation levels (high strength, low conductivity regime). This behavior can be readily understood by considering the role of volume fraction and morphology of the eutectic. Specifically, at low strains, the higher volume fraction of eutectic in the DS 55 alloy leads to a higher strength at a particular conductivity. Because the strain hardening and rod refinement of the DS 65 alloy is higher than in the DS 55 alloy, however, the amount of deformation necessary for a particular strength level in the DS 65 alloy is considerably less than in the DS 55 alloy. Consequently, the drop in conductivity is less pronounced leading to the behavior observed in Figure 55. When compared to the SCF results of Sakai and coworkers, the DS 65 alloy appears to have greater potential to provide greater strength at high deformation level. Figure 56 is a normalized UTS-conductivity plot obtained by multiplying the slope of each curve in Figure 55 by each data. The figure indicates that the DS 65 alloy with more rod-like interdendritic eutectic provides a better combination of strength and conductivity. This is basically due to the high decreasing rate in conductivity on deformation for lamellar-eutectic.

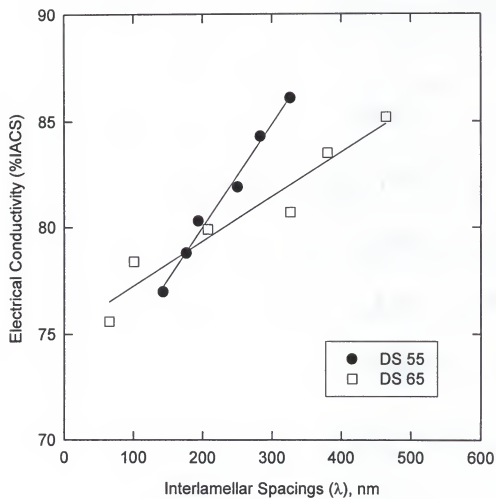


Figure 54. Electrical conductivity dependence on interlamellar spacings for the alloys with different eutectic morphology.

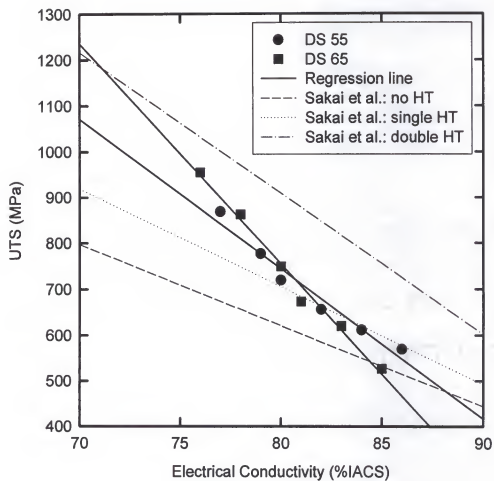


Figure 55. UTS dependence on conductivity for the alloys with different eutectic morphology.

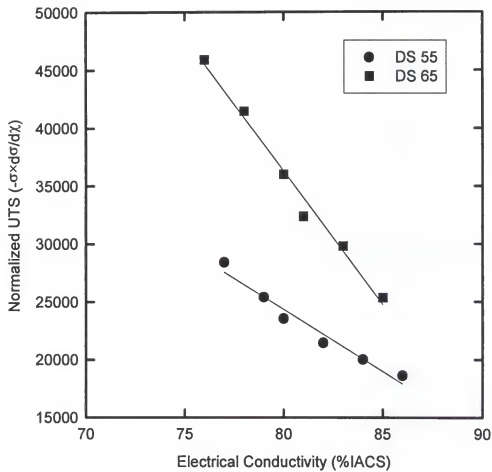


Figure 56. Normalized UTS dependence on conductivity for the alloys with different eutectic morphology.

4.5 Influence of Precipitation

Cu-Ag alloys can be strengthened by precipitation hardening. While the maximum strength will correspond to the maximum hardness, this condition normally has lower electrical conductivity than the overaged condition and may not provide the optimum combination of strength and conductivity. The overaged condition does not always provide higher electrical conductivity [126] than the other aging conditions because the conductivity presumably depends on the interface nature between precipitates and matrix as well as the size and distribution of the precipitates. Our interest was to determine the optimum tradeoff between strength increase and conductivity loss. Therefore, in this section, precipitation hardened specimens were compared and contrasted with those given no heat treatment specimen and those given only a "solution" treatment.

4.5.1 Peak Hardness Identification

The precipitation behavior of Cu-Ag alloys depends on the degree of pre-deformation (deformation before aging) as well as on the aging temperature and time. In order to identify the amount of pre-deformation and aging temperature providing the peak hardness level, microhardness tests were carried out on specimens aged for 1 h at various pre-deformation levels and aging temperatures. Figure 57 shows the hardness dependence on pre-deformation reduction of area for the DS 58 alloys aged for 1 h at various temperatures.

The overall hardness results from the combined effect of the strengthening by precipitation and that due to work hardening and subsequent recovery due to high aging temperature. The initial hardness increase is obviously the result of precipitation of solute atoms dissolved in the matrix. This precipitation effect is enhanced by TMP as shown in Figure 57 and appears to be maximum at 350 °C at 30-40% of RA. The variation of microhardness on aging temperature for the alloys with different pre-deformation levels is shown in Figure 58 where it is apparent that the higher the aging temperature, the larger the softening effect. Specimens with large pre-deformation levels have peak hardnesses at low aging temperatures (e.g., 300 °C). In these highly pre-deformed alloys, however, most of the strengthening results from the residual dislocations which were not annihilated at the lower aging temperature. Therefore, the maximum precipitation hardening will be obtained from the initial hardness increase condition, at which the strengthening by precipitation surpasses the recovery effect at the high aging temperatures. The hardness variation with both aging temperature and reduction of area (Figure 59 (a)) and the iso-hardness contours (Figure 59 (b)) indicate that the aging temperature and pre-deformation levels providing peak-hardness are 340-360 °C and 25-35 %RA, respectively. From these results the aging condition to provide maximum hardness can be determined as 350°C for 1h after cold working to 30%RA.

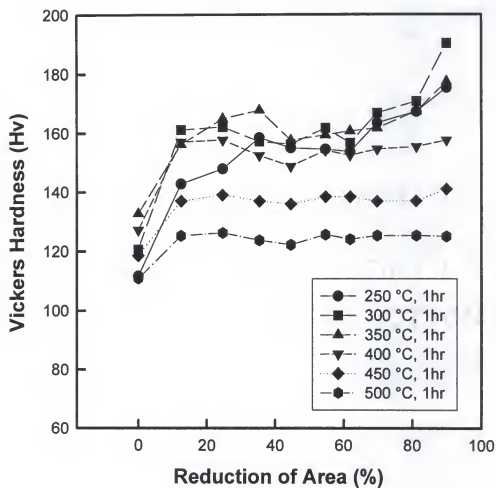


Figure 57. Microhardness vs. reduction of area (RA%) for the DS 58 alloy aged for 1 h at various temperatures.

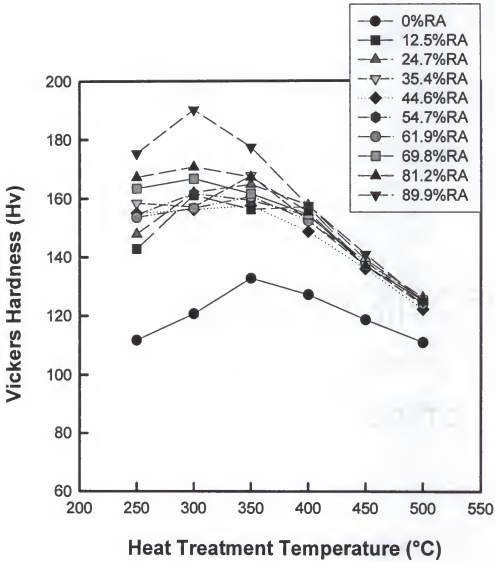
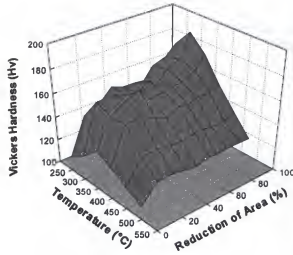
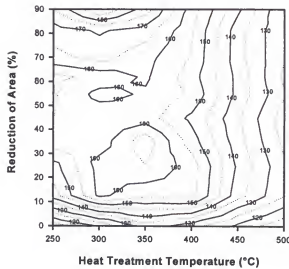


Figure 58. Microhardness variations with aging temperature for the DS 58 alloy aged for 1 h at various pre-deformation levels.



(a) 3-D view



(b) Iso-hardness contours

Figure 59. Microhardness variations with aging temperature and pre-deformation levels for the alloy aged for 1 h.

4.5.2 Aging Behavior and Prestrain Effect

Figure 60 shows the hardness variation with aging time at 350 °C for a chill cast Cu-10a/oAg alloy. Since the internal stress contains the components due to substructure (strain, grain boundaries, phase boundaries, precipitates, etc.), then the following expression can be used to qualitatively describe the behavior as appropriate to the current study:

$$\sigma = \sigma_0 + \sigma_{e1} + \sigma_{ppt} + \sigma_{e2} - \sigma_{ss} - \sigma_{rec} \quad (4-11)$$

where σ_0 is the stress increase due to the effect of friction and boundaries and σ_{e1} , σ_{ppt} , σ_{e2} , $-\sigma_{ss}$, and $-\sigma_{rec}$ are, respectively, the strength increases due to pre-aging deformation, precipitation, post-aging deformation and the strength drops due to the loss of solute atoms upon precipitation and recovery. Unlike normal age-hardening alloys, the formation of silver precipitates in copper require prestraining to produce appropriate nucleation sites due to the relatively high misfit ($\delta = +13\%$) between copper and silver. Consequently, the hardening response that results from aging will depend on the dislocation substructure which may undergo simultaneous recovery depending on the amount of pre-deformation prior to aging as well as the aging temperature. Figure 60 shows the Cu-3a/oAg alloy aged at 450 °C without prior deformation does not reveal an increase in the hardness.

It is true that the softening due to recovery is greater than the hardening due to precipitation for higher levels of prestrain and an overall reduction in strength occurs during aging as shown in Figure 57 and 58. The initial drop of hardness of the Cu-

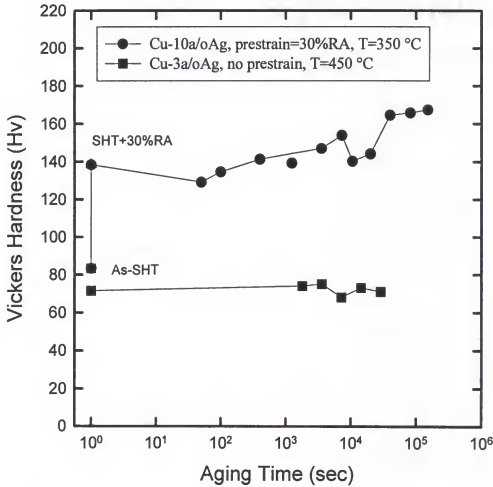


Figure 60. Aging behavior of Cu-3a/oAg alloy (aged at 450 °C with no prestrain) and Cu-10a/oAg alloy (aged at 350 °C after prestrain, 30%RA).

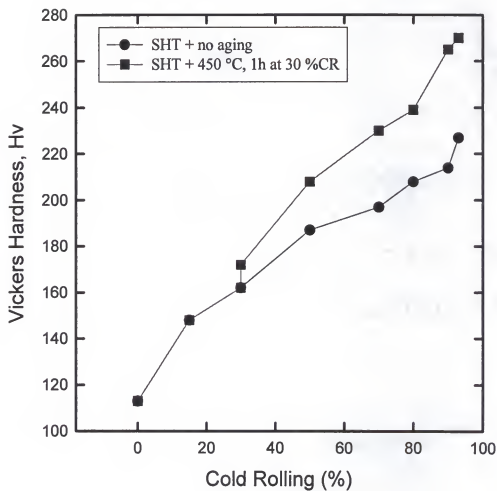
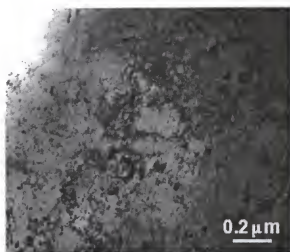


Figure 61. Effect of heat treatment on the hardness of Cu-12a/oAg alloy.

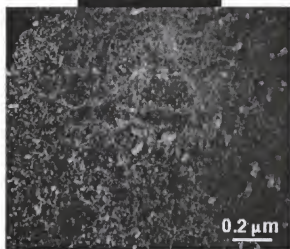
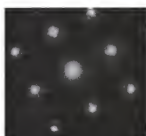
10a/oAg alloy aged at 350 °C in Figure 60 reflects that the recovery effect overrides the precipitation effect. The aging sequence of the Cu-10a/oAg (CS 10) alloy appears to be different from Cu-58a/oAg alloy because the hardness does not reach a peak value even for the specimen aged for 11 h at 350°C. Figure 61 shows the effect of heat treatment on the hardness of Cu-12a/oAg. The hardness increase after heat treatment at 450 °C for the pre-deformed specimen of 30% CR is due to precipitation of silver phase as will be shown in the next section. This means that the strength increase by precipitation is greater than the strength decrease due to recovery by dislocation annihilation, that is, $\sigma_{ppt} > -\sigma_{rec}$. Furthermore, the precipitation of silver combined with subsequent work hardening resulted in an increase in the overall hardness and hardening rate at low deformations as suggested by Sakai et al. [35].

4.5.3 Microstructure

TEM micrographs displaying the fine silver precipitates (2~4 nm) in the Cu-10Ag alloy after 30%RA and aging for 11.2 h at 350°C are shown in Figure 62. These precipitates have a cube-cube orientation relationship with the copper and is consistent with the early stages of decomposition in rapidly-quenched Cu-50a/oAg alloy foils undergoing Spinodal Decomposition [104]. The size of the silver precipitates in the Cu-12a/oAg alloy aged at 450 °C for 1 h after cold rolling to 30% reduction in thickness is increased to about 10 nm as shown in Figure 63. The corresponding diffraction pattern (Figure 63(a)) indicates that the cube-cube relationship between the two phases is not maintained as the precipitate size is increased. The shape of the silver precipitates is very irregular.

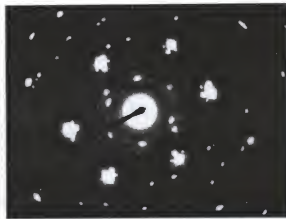
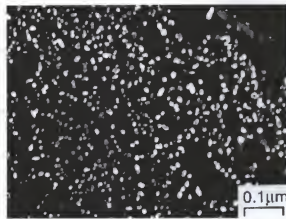


(a) BF

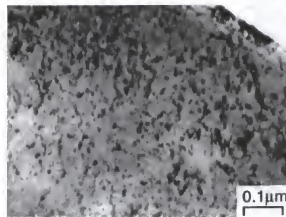


(b) CDF

Figure 62. TEM micrographs and SADP ($B=[001]$) showing fine silver phase precipitates in a copper matrix. (Cu-10a/oAg, 30%RA+350 °C, 11.2 hrs)

(a) $B_{Cu}=[114]$ 

(b) CDF



(c) BF

Figure 63. TEM micrographs of silver precipitates in a Cu-12a/oAg alloy aged at 450 °C for 1 h after 30% reduction by cold rolling.

4.5.4 Influence of Precipitation on Strength

The microstructure of Cu-10a/oAg alloy is composed of primary copper dendrites and interdendritic eutectic as shown in Figure 9. Therefore, the strength of this in-situ composite will be determined by the strength of the primary copper and interdendritic eutectic phases. Because the volume fraction of primary copper in Cu-10Ag alloy is about 89%, the total strength of this alloy, $\sigma_{\text{composite}}$ can be expressed in terms of two constituents by composite model [7, 17, 73, 127, 128] as follows;

$$\sigma_{\text{composite}} = f_{\text{Cu-primary}} \sigma_{\text{Cu-primary}} + f_{\text{eutectic}} \sigma_{\text{eutectic}} = 0.89 \sigma_{\text{Cu-primary}} + 0.11 \sigma_{\text{eutectic}} \quad (4-12)$$

where $\sigma_{\text{Cu-primary}}$ and $f_{\text{Cu-primary}}$ are the strength and volume fraction of the primary copper while σ_{eutectic} and f_{eutectic} those of the eutectic.

Figure 64 shows the tensile strength variation on the draw ratio where the TMP specimen is compared to the as-quenched and deformed specimen. The higher tensile strength of the TMP alloy is primarily due to the precipitation of silver in the copper matrix (σ_{ppt}) although copper might have precipitated in the eutectic silver phase as well. The reason for the lower hardening rate in the TMP specimen is unclear. It appears that the strength of the TMP specimen does not follow the exponential equation suggested by Spitzig et al. [94].

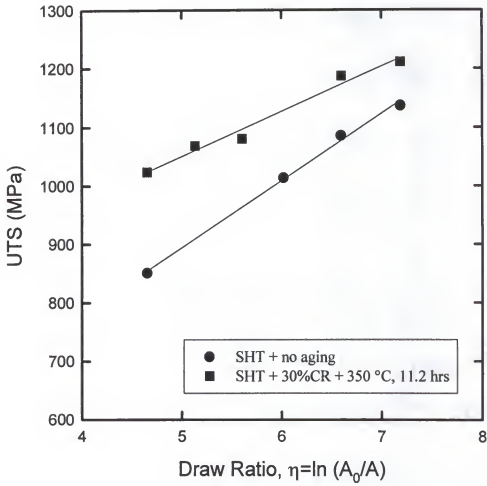


Figure 64. UTS vs. draw ratio for the Cu-10Ag alloy with and without an intermediate aging treatment.

4.5.5 Influence of Precipitation on Electrical Conductivity

The variation of electrical conductivity on the deformation of TMP specimens is shown in Figure 65 where the conductivity data of the DS 58 alloy are also presented for comparison. The sensitivity of the conductivity to deformation of the TMP specimens is lower than the DS 58 alloy which means that the interface effect is the most detrimental in reducing electrical conductivity than any other scattering source of free electrons. Surprisingly, the solute effect on conductivity is not as detrimental as the interface effect.

The dependence of electrical conductivity with draw ratio for the DS 58 alloys (0, 45 and 90° orientation) aged to peak hardness condition is shown in Figure 66. The electrical conductivity decreases more rapidly compared with similar alloys without heat treatment (see Figure 34); this suggests that precipitation accelerates the conductivity drop at all misorientation especially the 0° specimens. Figure 67 shows that the sensitivity of electrical conductivity on deformation for TMP specimens is much higher than the one with no HT and the value is decreased linearly as the initial misorientation increases. Therefore, we can say

$$|d\chi/d\eta|_{\text{NHT}} < |d\chi/d\eta|_{\text{HT}} = kf(\phi) \quad (4-13)$$

Precipitation of silver or copper phases dilutes the misorientation dependence of electrical conductivity of the DS 58 alloy at different draw ratios as indicated in Figures 68 and 69. By comparison with Figure 39, it is clear that

$$(d\chi/d\phi)_{\text{NHT}} > (d\chi/d\phi)_{\text{HT}} = k'f(\eta) \quad (4-14)$$

This implies that the relative misorientation effect at high draw ratios is also decreased by the effect of precipitates as shown in Figure 69.

4.6 Influence of Composition

The dependence of the SCF on composition is plotted in Figure 70. Clearly, the off-eutectic alloys exhibit higher SCF values although there were some variations on the withdrawal speed for each DS alloy. The larger interlamellar spacing also contributes to the increase in SCF values. The growth morphology of a eutectic also influences the SCF values, namely, the DS 65 alloy with the rod-like interdendritic eutectic exhibited higher SCF values than the DS 55 alloy with more lamellar-like eutectic. The results, however, should involve a combined effect of off-eutectic composition because the DS 65 alloy contains a higher volume fraction of primary phases than that of the DS 55 alloy. Therefore, it can be concluded that the dominant factors determining the value of SCF are the relative volume fraction and interlamellar spacing of the eutectic phase, together with their growth morphology.

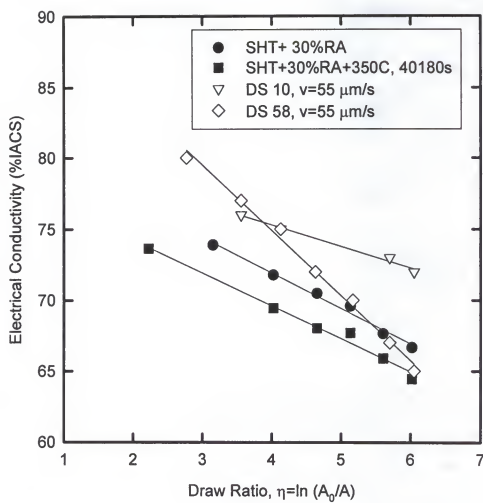


Figure 65. Variation in the electrical conductivity on draw ratio of the TMP Cu-10Ag alloys as well as the DS 10 and DS 58 alloys.

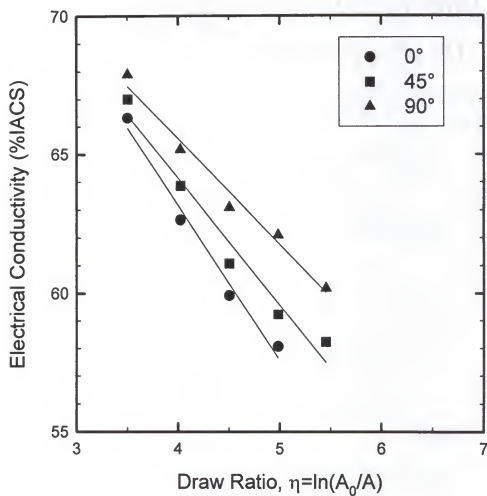


Figure 66. The dependence of electrical conductivity on draw ratio for the aged DS 58 alloy with different initial deviations from the growth axis.

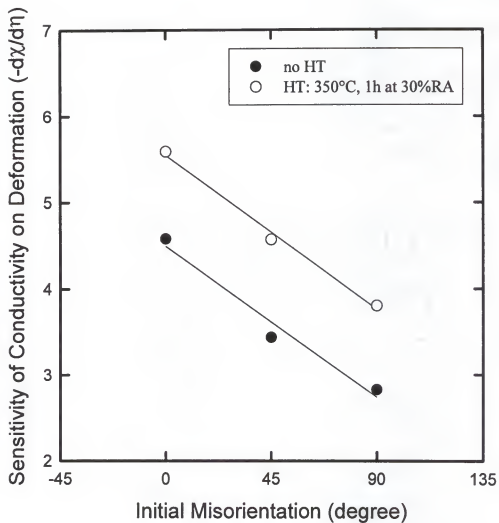


Figure 67. The variation of the deformation sensitivity of electrical conductivity on initial misorientation of eutectic relative to the drawing axis for the DS 58 alloy.

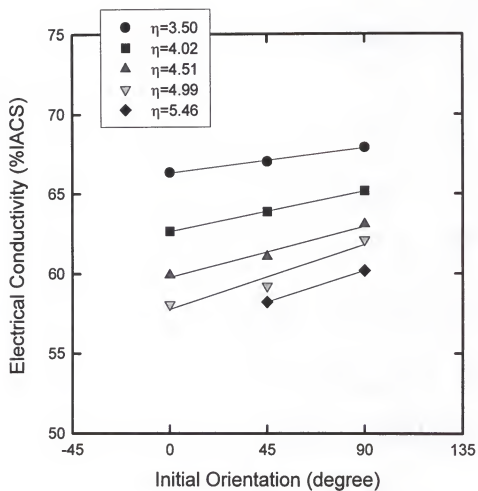


Figure 68. The dependence of electrical conductivity on initial orientation for the aged DS 58 alloys at various deformation levels.

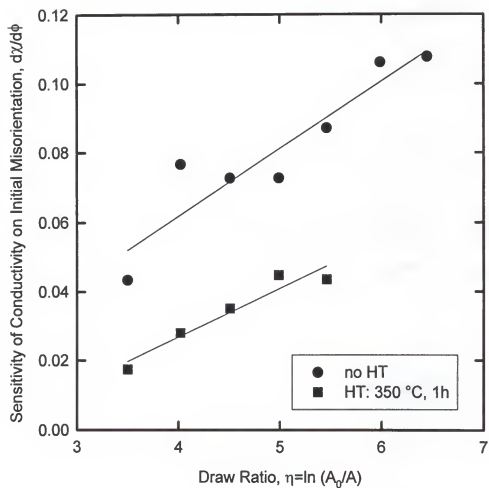


Figure 69. Rate of change of the sensitivity of conductivity for the DS 58 alloys on initial misorientation at various deformation levels; the data are normalized by the properties at $\eta=3.5$.

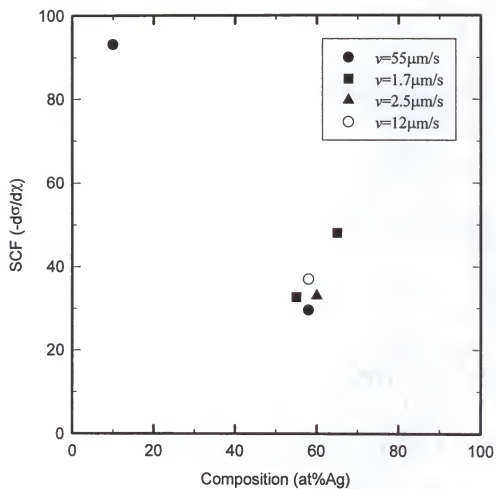


Figure 70. The variation of SCF with silver content in the Cu-Ag alloys.

CHAPTER 5 CONCLUSIONS

5.1 Influence of the Volume Fraction of Eutectic Constituent

- (1) The tensile strength vs. draw ratio for the Cu-Ag microcomposites follows the exponential relationship suggested by Spitzig for Cu-Nb alloys.
- (2) The increased volume fraction of eutectic constituents increases the strength of the Cu-Ag alloy but has little effect on the hardening rate. This means that the interphase interfaces in the Cu-Ag alloys are not as effective for strengthening when compared with the Cu-BCC systems (e.g., Cu-Nb).
- (3) The increased interfacial area of the eutectic phases cause a decrease in the conductivity of the eutectic alloy more rapidly than that of an off-eutectic alloy containing less interfacial area. At low draw ratios (relatively high interlamellar spacings), the volume fraction of the high conductivity phase (silver) is a dominant factor determining the total conductivity. However, with the increase in the deformation level, the amount of interfacial area becomes the more important factor especially when the interlamellar spacing gets close to the mean free path of electrons in each phase.
- (4) While the increase in interfacial area increases the strength only a small amount, it decreases the conductivity significantly (low SCF). Therefore, interface strengthening is not an effective way of improving both the strength and conductivity of Cu-Ag alloys. This is basically due to the detrimental effect of the

interface on the conductivity when the thickness of the lamellae becomes close to the mean free path of free electrons.

5.2 Influence of Interlamellar Spacing (λ) of Eutectic

- (1) Neither the Cu or Ag phases show any preferential deformation behavior in the composite: each Cu or Ag lamellar plate suffers similar deformation with that of the bulk wire of the same composition.
- (2) The drawn CS 58 alloy has a wavy microstructure due to the different orientations of neighboring colonies and the preferred orientation of the interphase interface, whereas the eutectics in the DS alloys tend to be very straight at similar deformation levels.
- (3) While eutectic alloys with smaller interlamellar spacings have higher strengths than those with larger spacings, the alloys with larger interlamellar spacing tend to have higher work hardening rates.
- (4) Smaller interlamellar spacings result in an increase in the sensitivity of the conductivity on the draw ratio: as the initial interlamellar spacing becomes smaller, the conductivity of the eutectic decreases more rapidly with deformation level due to the increased effect of the interfaces.
- (5) The alloys with larger initial interlamellar spacings exhibit better combinations of strength and conductivity at high deformation levels. On the contrary, the alloy with smaller interlamellar spacings exhibit better combinations at lower deformation levels.

5.3 Influence of Initial Orientation of Lamellae

- (1) Specimens cut parallel to the growth axis exhibit the highest tensile strengths and lowest electrical conductivities at a given deformation level.
- (2) The hardening rate did not vary significantly with initial orientation.
- (3) The conductivity decrease with draw ratio was the greatest for the 0° specimen.
The necessary reorientation of the lamellae in the 90° specimen reduced the sensitivity of electrical conductivity on the interlamellar spacing and thus improved the SCF values.
- (4) The strength sensitivity on electrical conductivity (SCF) is a linear function of misorientation and is highest when the misorientation is maximum (90°). This means that an eutectic alloy with randomly oriented eutectic colonies provides better SCF values than that with unidirectionally aligned structures.
- (5) The sensitivity of strength on the initial misorientation is constant, while the sensitivity of conductivity depends on the amount of deformation. The increased sensitivity of conductivity on misorientation at high deformation level indicates that the reduced interlamellar spacing is a critical factor reducing the electrical conductivity.

5.4 Influence of Growth Morphology of Interdendritic Eutectic

- (1) The primary phase present in the off-eutectic alloys results in a change in the morphology of the interdendritic eutectic near these primary phases. However, this morphological change is limited to the regions adjacent to the primary phase.

- (2) The interdendritic eutectic far away from the primary copper in the DS 55 alloy appears to be more lamellar while that of the DS 65 alloy more rod-like. The differences in the morphology are the result of localized coupled-growth of the interdendritic eutectic due to the reduced average silver content in liquid under the imposed experimental conditions.
- (3) The difference in eutectic morphology leads to different hardening rates during drawing with the lamellar eutectic providing a higher hardening rate. However, the rod-like eutectic in the DS 65 alloy experiences greater overall refinement in microstructural scale; this overwhelms the hardening of the lamellar eutectic in the DS 55 alloy.
- (4) At lower strains, the volume fraction of eutectic (assuming the same interlamellar spacing) is the more dominant factor determining the total strength of the material whereas, at higher strains, the greater refinement of the rod-like eutectic as well as the size of the interlamellar spacing (morphology-induced) becomes dominant.
- (5) The interlamellar spacing of the interdendritic eutectic is responsible for the lower electrical conductivity of the DS 65 alloy at the high deformation levels. However, the morphological effect is a major factor lowering the electrical conductivity of the DS 65 alloy at low deformation levels.
- (6) The fully lamellar eutectic alloy has a higher sensitivity of electrical conductivity on interlamellar spacing, λ , and the lamellar eutectic greatly reduces the electrical conductivity especially when the interlamellar spacings approach the mean free path of electrons in the constituent phases.

5.5 Influence of Precipitation

- (1) A peak in hardness in isochronal (1h) aging experiments was observed at $\sim 350^{\circ}\text{C}$ after predeforming to 25-35%RA for a eutectic alloy. At higher temperatures, the material undergoes recovery, where the precipitation effect overpasses the recovery due to high aging temperature.
- (2) Precipitation accelerates the conductivity drop at all misorientations, especially for the 0° samples.
- (3) Precipitation of the silver or copper phases dilutes the misorientation dependence of electrical conductivity of the DS 58 alloy.

5.6 Influence of Composition

- (1) The Cu-Ag alloys with off-eutectic compositions have higher SCF values than their eutectic alloys.
- (2) The relative volume fraction and interlamellar spacing of the eutectic phase together with the growth morphology are dominant factors determining the SCF values.

LIST OF REFERENCES

1. Crow, J. E., Parkin, D. M., and Sullivan, N. S., Materials science in high magnetic fields, *MRS Bulletin*, 18 (1993), 17-21.
2. Miura, N. and Goto, T., High field applications- Megagauss field generation by condenser discharge and its application to solid state physics, in *Megagauss Fields and Pulsed Power Systems*, V.M. Titov and G.A. Shvetsov, 1990, Nova Science Publishers Inc., New York, 119-138.
3. Campbell, L., The National High Magnetic Field Laboratory-Overview, in *Los Alamos National Laboratory Report*, 1995, Summer, Los Alamos, New Mexico.
4. Dew-Hughes, D., High strength conductor for pulsed magnets, *Materials Science and Engineering*, A168 (1993), 35-40.
5. Dupouy, F., Askénazy, S., Peyrade, J. P., and Legat, D., Composite conductors for high pulsed magnetic fields, *Physica B*, 211 (1995), 43-45.
6. Bevk, J., Harbison, J. P., and Bell, J. L., Anomalous increase in strength of in situ formed Cu-Nb multifilamentary composites, *Journal of Applied Physics*, 49 (1978), 6031-6038.
7. Frommeyer, G. and Wassermann, G., Microstructure and anomalous mechanical properties of in situ-produced silver-copper composite wires, *Acta Metallurgica*, 23 (1975), 1353-1360.
8. Spitzig, W. A. and Krotz, P. D., A comparison of the strength and microstructure of heavily cold worked Cu-20% Nb composites formed by different melting procedures, *Scripta Metallurgica*, 21 (1987), 1143-1146.
9. Karasek, K. R. and Bevk, J., Normal-state resistivity of in situ-formed ultrafine filamentary Cu-Nb composite, *Journal of Applied Physics*, 52 (1981), 1370-1375.
10. Bevk, J., Sunder, W. A., Dublon, G., and Cohen, D. E., Mechanical properties of Cu-based composites with in situ formed ultrafine filaments, in *In Situ Composites IV*, F.D. Lemkey, H.E. Cline, and M. McLean, 1982, Elsevier Science Publishing Co. Inc., Amsterdam, 121-133.

11. Verhoeven, J. D., Downing, H. L., Chumbley, L. S., and Gibson, E. D., The resistivity and microstructure of heavily drawn Cu-Nb alloys, *Journal of Applied Physics*, 65 (1989), 1293-1301.
12. Trybus, C. L. and Spitzig, W. A., Characterization of the strength and microstructural evolution of a heavily cold rolled Cu-20% Nb composite, *Acta Metallurgica*, 37 (1989), 1971-1981.
13. Spitzig, W. A. and Reed, L. K., Temperature and strain rate dependence of the strength of heavily cold-drawn copper, niobium and Cu-20%Nb, *Materials Science and Engineering*, A111 (1989), L13-L17.
14. Noto, K., Matsukawa, M., Takahashi, C., Konno, H., Saito, Y., *et al.*, High-conductivity high-strength Cu-Nb composites, *Cryogenics*, 30 (1990), 383-387.
15. Pourrahi, S., Nayeb-Hashemi, H., and Foner, S., High-strength high-conductivity Cu-Nb microcomposite wire by powder metallurgy, *Journal of Materials Science Letters*, 2 (1990), 1484-1487.
16. Klein, J. D., Cogan, S. F., Yen, A., and Wu, L. L., Metal-metal microfilamentary composites for high strength electrical conductor applications- Phase II, DNA-TR-90-170, 1991, Defence Nuclear Agency, Alexandria, Virginia.
17. Verhoeven, J. D., Chumbley, L. S., Laabs, F. C., and Spitzig, W. A., Measurement of filament spacing in deformation processed Cu-Nb alloys, *Acta Metallurgica et Materialia*, 39 (1991), 2825-2834.
18. Spitzig, W. A., Strengthening in heavily deformation processed Cu-20% Nb, *Acta Metallurgica et Materialia*, 39 (1991), 1085-1090.
19. Chumbley, L. S. and Laabs, F. C., Observation of Nb filaments in Cu-Nb in-situ composites, *Scripta Metallurgica et Materialia*, 25 (1991), 2097-2101.
20. Pourrahi, S., Nayeb-Hashemi, H., and Foner, S., Strength and microstructure of powder metallurgy processed restacked Cu-Nb microcomposites, *Metallurgical Transactions A*, 23A (1992), 573-586.
21. Vance, R. R. and Courtney, T. H., Hot isostatic pressing of mechanically alloyed Cu-Nb powders, *Scripta Metallurgica et Materialia*, 26 (1992), 1435-1440.
22. Zeik, K. L., Koss, D. A., Anderson, I. E., and Howell, P. R., Microstructural evolution and thermal stability associated with a gas-atomized Cu-Nb alloy, *Metallurgical Transactions A*, 23A (1992), 2159-2167.
23. Jha, S. C., Delagi, R. G., Forster, J. A., and Krotz, P. D., High-strength high-conductivity Cu-Nb microcomposite sheet fabricated via multiple roll bonding, *Metallurgical Transactions A*, 24A (1993), 15-20.

24. Ellis, T. W., Anderson, I. E., Downing, H. L., and Verhoeven, J. D., Deformation-processed wire prepared from gas-atomized Cu-Nb alloy powders, *Metallurgical Transactions A*, 24A (1993), 21-26.
25. Spitzig, W. A., Downing, H. L., Laabs, F. C., and Verhoeven, J. D., Strength and electrical conductivity of a deformation-processed Cu-5 pct Nb composite, *Metallurgical Transactions A*, 24A (1993), 7-14.
26. Jones, H., Schneider-Muntau, H. J., and Herlach, F., Pulsed single and multisection magnets using various wires including CuNb microcomposite, *IEEE Transactions on Magnetics*, 30 (1994), 1651-1656.
27. Nikulin, A. D., Shikov, A. K., Pantsyrny, V. I., Vorobjova, A. E., Dergunaova, E. A., *et al.*, Investigation of electrophysical and mechanical properties of high-strength Cu-Nb composites for pulse magnetic system winding wires, *IEEE Transactions on Magnetics*, 30 (1994), 2395-2398.
28. Heremans, G., Van Bockstal, L., Liang, L., Herlach, F., Nikulin, A., *et al.*, Fibre composites combined with matched high strength Cu-Nb microfilament conductors for high performance pulsed magnets, *IEEE Transactions on Magnetics*, 30 (1994), 2180-2183.
29. Renaud, C. V., CuNb wire development at Supercon Inc., in *National High Magnetic Field Laboratory Workshop-- High-Strength High Conductivity Composite Materials*, 1994, August 18-19, Tallahassee, Florida.
30. Raabe, D., Heringhaus, F., Hangen, U., and Gottstein, G., Investigation of a Cu-20 mass% Nb in situ composite- Part I: Fabrication, Microstructure and Mechanical Properties, *Zeitschrift fur Metallkunde*, 86 (1995), 405-415.
31. Henne, M. L. and Ebrahimi, F., The processing and deformation of a rapidly solidified CuNb alloy, in *The TMS Fall Meeting*, 1995, October 29-November 2, Cleveland, Ohio.
32. Hong, S. I., Hill, M. A., Sakai, Y., Wood, J. T., and Embury, J. D., On the stability of cold drawn, two-phase wires, *Acta Metallurgica et Materialia*, 43 (1995), 3313-3323.
33. Raabe, D., Heringhaus, F., Hangen, U., and Gottstein, G., Investigation of a Cu-20 mass% Nb in situ composite- Part II: Electromagnetic properties and application, *Zeitschrift fur Metallkunde*, 86 (1995), 416-422.
34. Heringhaus, F., Raabe, D., and Gottstein, G., On the correlation of microstructure and electromagnetic properties of heavily cold worked Cu-20% Nb wires, *Acta Metallurgica et Materialia*, 43 (1995), 1467-1476.

35. Sakai, Y., Inoue, K., Asano, T., Wada, H., and Maeda, H., Development of high-strength high-conductivity Cu-Ag alloys for high-field pulsed magnet use, *Applied Physics Letters*, 59 (1991), 2965-2967.
36. Schneider-Muntau, H. J., The generation of quasistationary fields up to 100T, *IEEE Transactions on Magnetics*, 24 (1988), 1045-1048.
37. Gersdorf, R., Roeland, L. W., and Mattens, W. C. M., A magnet for semi-continuous fields upto 60T, *IEEE Transactions on Magnetics*, 24 (1988), 1052-1054.
38. Herlach, F., The technology of pulsed high field magnets, *IEEE Transactions on Magnetics*, 24 (1988), 1049-1051.
39. Schneider-Muntau, H. J., The generation of high D.C. magnetic fields, *IEEE Transactions on Magnetics*, 24 (1988), 1041-1044.
40. Turowski, P. and Schneider, T., 19.3 T with a superconducting magnet, *IEEE Transactions on Magnetics*, 24 (1988), 1063-1066.
41. Asano, T., Sakai, Y., Inoue, K., Oshikiri, M., and Maeda, H., High-field pulsed magnet wound of Cu-Ag alloy wire, *Japanese Journal of Applied Physics*, 32 (1993), L1207-L1209.
42. Noto, K., Matsukawa, M., Katagiri, K., Iwabuchi, A., Sato, T., *et al.*, Reinforcing stabilizers for large scale and/or high field superconducting magnets, *Fusion Engineering and Design*, 20 (1993), 455-462.
43. Gao, B. J., Bird, M. D., Eyssa, Y. M., and Schneider-Muntau, H. J., Material and cooling requirements for Poly-Bitter resistive magnets and hybrid inserts generating continuous fields up to 50T, *IEEE Transactions on Magnetics*, 30 (1994), 2196-2199.
44. Kiyoshi, T., Inoue, K., Itoh, K., Takeuchi, T., Oshikiri, M., *et al.*, Operation of a 20-T superconducting magnet with a large bore, *IEEE Transactions on Magnetics*, 30 (1994), 2110-2113.
45. Bird, M. D., Bole, S., Eyssa, Y. M., Gao, B. J., Zhang, H., *et al.*, Design of resistive inserts for the NHMFL 45-T hybrid magnet, *IEEE Transactions on Magnetics*, 30 (1994), 2192-2195.
46. Miller, J. R., Bird, M. D., Bole, S., Botino-Oliva, A., Eyssa, Y. M., *et al.*, An overview of the 45-T hybrid magnet system for the new National High Magnetic Field Laboratory, *IEEE Transactions on Magnetics*, 30 (1994), 1563-1571.
47. Van Sciver, S. W., NHMFL Reports--The cryogenic system for the NHMFL hybrid magnet, 1995, National High Magnetic Field Laboratory, Tallahassee, Florida.

48. Embury, J. D., Hill, M. A., Spitzig, W. A., and Sakai, Y., Microstructural aspects of materials for nondestructive long-pulse high-field magnets, *MRS Bulletin*, 18 (1993), 57-60.
49. Schneider-Muntau, H. J., Nondestructive megagauss fields, in *Megagauss Fields and Pulsed Power Systems*, V.M. Titov and G.A. Shvetsov, 1990, Nova Science Publishers Inc., New York, 99-106.
50. Herlach, F., Research with pulsed magnetic fields from the early beginnings to future prospects, in *Megagauss Fields and Pulsed Power Systems*, V.M. Titov and G.A. Shvetsov, 1990, Nova Science Publishers Inc., New York, 15-20.
51. Heremans, G., Herlach, F., Van Bockstal, L., Witters, J., and Lefever, I., High performance coils for pulsed magnets, *IEEE Transactions on Magnetics*, 28 (1992), 790-793.
52. Pernambuco-Wise, P., Materials for pulse magnet application, in *National High Magnetic Field Laboratory Workshop-- High-Strength High Conductivity Composite Materials*, 1994, August 18-19, Tallahassee, Florida.
53. Eyssa, Y. M., Gao, B. J., and Bird, M. D., Material requirements for resistive magnets at the NHMFL, in *National High Magnetic Field Laboratory Workshop-- High-Strength High Conductivity Composite Materials*, 1994, August 18-19, Tallahassee, Florida.
54. Jones, H., Herlach, F., Lee, J. A., Whitworth, H. M., Day, A. G., *et al.*, 50 Tesla pulsed magnets using a copper conductor externally reinforced with stainless steel, *IEEE Transactions on Magnetics*, 24 (1988), 1055-1058.
55. Morris, M. A. and Morris, D. G., Microstructures and mechanical properties of rapidly solidified Cu-Cr alloys, *Acta Metallurgica*, 35 (1987), 2511-2522.
56. Dahmen, U., Witcomb, M. J., and Westmacott, K. H., Morphology of Cr precipitates in an overaged Cu-0.3%Cr alloy, *Scripta Metallurgica*, 22 (1988), 1867-1872.
57. Ellis, D. L. and Michal, G. M., Formation of Cr and Cr₂Nb precipitates in rapidly solidified Cu-Cr-Nb ribbon, *Ultramicroscopy*, 30 (1989), 210-216.
58. Takeuchi, T., Togano, K., Inoue, K., and Maeda, H., Fibrous chromium and molybdenum fabricated by cold working Cu-Cr and Cu-Mo binary alloys, *Journal of the Less-Common Metals*, 157 (1990), 25-35.
59. Verhoeven, J. D., Spitzig, W. A., L., J. L., Downing, H. L., Trybus, C. L., *et al.*, Development of deformation processed copper-refractory metal composite alloys, *Journal of Materials Engineering*, 12 (1990), 127-139.

60. Ellis, D. L. and Michal, G. M., Production and processing of Cu-Cr-Nb alloys, *Scripta Metallurgica et Materialia*, 24 (1990), 885-890.
61. Malzahn Kampe, J. C., Cooper, K. P., and Ayers, J. D., Deformation processed composite wires from gas-atomized Cu-Cr-Ag powder, *Scripta Metallurgica*, 24 (1990), 1783-1788.
62. Berge, P. M., Haupt, G. R., Gibson, E. D., and Verhoeven, J. D., A new high strength high conductivity copper alloy wire, *Wire Journal International*, 24 (1991), 62-65.
63. Juarez-Islas, J. A., Perez, R., Albarran, L. A., Rivera, V., and Martinez, L., Development of high-strength high-conductivity copper alloys by rapid solidification, *Journal of Materials Science Letters*, 11 (1992), 1104-1106.
64. Fritzemeier, L. G., High strength high conductivity composites, *Nanostructured Materials*, 1 (1992), 257-262.
65. Biselli, C. and Morris, D. G., High strength-high conductivity fibre-reinforced copper alloys, *Journal de Physique IV: Colloque C7*, 3 (1993), 1737-1740.
66. Hardwick, D. A., Rhodes, C. G., and Fritzemeier, L. G., The effect of annealing on the microstructure and mechanical properties of Cu-X microcomposites, *Metallurgical Transactions A*, 24A (1993), 27-34.
67. Anderson, K. R., Groza, J. R., Dreshfield, R. L., and Ellis, D., Microstructural evolution and thermal stability of precipitation-strengthened Cu-8Cr-4Nb alloy, *Materials Science and Engineering*, A169 (1993), 167-175.
68. Anderson, K. R., Groza, J. R., Dreshfield, R. L., and Ellis, D., High-performance dispersion-strengthened Cu-8 Cr-4 Nb alloy, *Metallurgical and Materials Transactions A*, 26A (1995), 2197-2206.
69. Spitzig, W. A. and Krotz, P. D., Comparison of the strengths and microstructures of Cu-20% Ta and Cu-20% Nb in situ composites, *Acta Metallurgica*, 36 (1988), 1709-1715.
70. Verhoeven, J. D., In situ composites prepared by solidification and mechanical techniques, in *In Situ Composites IV*, 1981, November, Boston, Massachusetts, 267-276.
71. Funkenbusch, P. D. and Courtney, T. H., On the strength of heavily cold worked in-situ composites, *Acta Metallurgica*, 33 (1985), 913-922.
72. Jerman, G. A., Anderson, I. E., and Verhoeven, J. D., Strength and electrical conductivity of deformation-processed Cu-15vol pct Fe alloys produced by powder metallurgy techniques, *Metallurgical Transactions A*, 24A (1993), 35-42.

73. Biselli, C. and Morris, D. G., Microstructure and strength of Cu-Fe in situ composites after very high drawing strains, *Acta Materialia*, 44 (1996), 493-504.
74. Ratka, J. O. and Spiegelberg, W. D., A high performance beryllium copper alloy for magnet application, *IEEE Transactions on Magnetics*, 30 (1994), 1859-1862.
75. Sims, J. R., Hill, M. A., and Walsh, R. P., Developments in materials for high-field magnets, *IEEE Transactions on Magnetics*, 30 (1994), 2211-2213.
76. Walder, S. and Ryder, P. L., Nonequilibrium solidification in undercooled melts of the alloy Ag-39.9 at.% Cu, *Journal of Applied Physics*, 73 (1965), 1965-1970.
77. Cline, H. E. and Stein, D. F., Strengthening by interfaces in the Ag-Cu directionally solidified eutectic, *Transactions of the Metallurgical Society of AIME*, 245 (1969), 841-846.
78. Cline, H. E. and Lee, D., Strengthening of lamellar vs. equiaxed Ag-Cu eutectic, *Acta Metallurgica*, 18 (1970), 315-323.
79. Frommeyer, G. and Wassermann, G., Anomalous properties of in-situ produced silver-copper composite wires I- Electrical conductivity, *Physica Status Solidi (a)*, 27 (1975), 99-105.
80. Frommeyer, G. and Brion, H. G., Hall effect in directionally solidified and deformed eutectic silver-copper alloys with fiber structure, *Physica Status Solidi (a)*, 66 (1981), 559-564.
81. Murray, J. L., Calculations of stable and metastable equilibrium diagrams of the Cu-Ag and Cd-Zn systems, *Metallurgical Transactions A*, 15A (1984), 261-268.
82. Davidson, C. J. and Smith, I. O., Interphase orientation relationships in directionally solidified silver-copper eutectic alloy, *Journal of Materials Science Letters*, 3 (1984), 759-762.
83. Manna, I. and Pabi, S. K., A study of the nucleation characteristics of discontinuous precipitation in a pro-eutectic Cu-Ag alloy, *Journal of Materials Science Letters*, 2 (1990), 1226-1228.
84. Manna, I. and Pabi, S. K., Effect of surface strain on discontinuous precipitation kinetics in a Cu-7.7at% Ag alloy, *Journal of Materials Science Letters*, 13 (1994), 62-64.
85. Sohn, K. Y. and Kaufman, M. J., Copper-silver microcomposites: Novel processing approaches, in *National High Magnetic Field Laboratory Workshop-- High-Strength High Conductivity Composite Materials*, 1994, August 18-19, Tallahassee, Florida.

86. Hirota, T., Imai, A., Kumano, T., Ichihara, M., Sakai, Y., *et al.*, Development of Cu-Ag alloys conductor for high field magnet, *IEEE Transactions on Magnetics*, 30 (1994), 1891-1894.
87. Rao, G., Howe, J. M., and Wynblatt, P., Analysis of the interfacial structure of a twinned variant of Ag precipitate in Cu-Ag alloys, *Scripta Metallurgica et Materialia*, 30 (1994), 731-736.
88. Asano, T., Sakai, Y., Oshikiri, M., Inoue, K., Maeda, H., *et al.*, Cu-Ag wire pulsed magnets with and without internal reinforcements, *IEEE Transactions on Magnetics*, 30 (1994), 2106-2109.
89. Sakai, Y., Inoue, K., and Maeda, H., High-strength and high-conductivity Cu-Ag sheets: New promising conductor for high field Bitter coils, *IEEE Transactions on Magnetics*, 30 (1994), 2114-2117.
90. Spitzig, W. A., Wheelock, P. B., Ellis, T. W., and Laabs, F. C., High strength/high conductivity Cu-7 vol%Ag- 12 vol%Nb wire, in *National High Magnetic Field Laboratory Workshop-- High-Strength High Conductivity Composite Materials*, 1994, August 18-19, Tallahassee, Florida.
91. Sakai, Y., Inoue, K., and Maeda, H., New high-strength high-conductivity Cu-Ag alloy sheets, *Acta Metallurgica et Materialia*, 43 (1995), 1517-1522.
92. Sohn, K. Y. and Kaufman, M. J., The effect of initial orientation of the eutectic lamellae on the strength and electrical conductivity of Cu-Ag microcomposites, in *The TMS fall meeting*, 1995, October 29-November 2, Cleveland convention center, Cleveland, OH.
93. Sohn, K. Y. and Kaufman, M. J., The strength and conductivity of Cu-Ag microcomposites produced by directional solidification, in *TMS Annual Meeting & Exhibit*, 1995, February 12-16, Las Vegas, Nevada.
94. Spitzig, W. A., Pelton, A. R., and Laabs, F. C., Characterization of the strength and microstructure of heavily cold worked Cu-Nb composites, *Acta Metallurgica*, 35 (1987), 2427-2442.
95. Foner, S., 68.4-T-long pulse magnet: Test of high strength microcomposite Cu/Nb conductor, *Applied Physics Letters*, 49 (1986), 982-983.
96. Foner, S., Bobrov, E., Renaud, C. V., Gregory, E., and Wong, J., 68.4T pulsed magnet fabricated with a wire-wound metal-matrix Cu/Nb microcomposite, *IEEE Transactions on Magnetics*, 24 (1988), 1059-1062.

97. Sakai, Y., Inoue, K., Asano, T., and Maeda, H., Development of a high strength high conductivity copper-silver alloy for pulsed magnets, *IEEE Transactions on Magnetics*, 28 (1992), 888-891.
98. Rose, R. M., Shepard, L. A., and Wulff, J., *Electronic Properties, The Structure and Properties of Materials*, ed. J. Wulff, 4, 1966, John Wiley & Sons, New York.
99. Pandey, O. P., Lele, S., and Ojha, S. N., Undercooling and solidification of droplets of Cu-Ag alloy entrained in the primary phase, *Journal of Materials Science*, 30 (1995), 538-543.
100. Elliott, R. P. and Giessen, W. C., The Ag-Cu (silver-copper) system, *Bulletin of alloy phase diagrams*, 1 (1980), 41-45.
101. Massalski, T. B., ed. *Binary alloy phase diagrams, Vol. 1 & 2*, 1986, American Society for Metals, Metals Park, Ohio.
102. Stoering, R. and Conrad, H., Metastable structures in liquid quenched and vapor quenched Ag-Cu alloys, *Acta Metallurgica*, 17 (1969), 933-948.
103. Elliott, W. A., Gagliano, F. P., and Krauss, G., Metastable phase produced by laser melt quenching, *Metallurgical Transactions*, 4 (1973), 2031-2037.
104. Boswell, P. G. and Chadwick, G. A., The structure of the γ' extended solid solution in a splat-cooled Ag-50at% Cu alloy, *Journal of Materials Science*, 12 (1977), 1879-1894.
105. Ebrahimi, F., Development of Cu-based composites: An optimization of strength and electrical conductivity, in *National High Magnetic Field Laboratory Workshop - High-Strength High Conductivity Composite Materials*, 1994, August 18-19, Tallahassee, Florida.
106. Kurz, W. and Fisher, D. J., Dendrite growth in eutectic alloys: the coupled zone, *International Metals Review*, 24 (1979), 177-204.
107. Frommeyer, G. and Schneider, K. F., Size effect and interface contribution to diamagnetism of silver-copper composite wires with fibre structure, *Physica Status Solidi (a)*, 41 (1977), 653-658.
108. Nagakura, S., Toyama, S., and Oketani, S., Lattice parameter and structure of silver-copper alloys rapidly quenched from liquid state, *Acta Metallurgica-Letter*, 14 (1966), 73-75.
109. Boettinger, W. J., Schaefer, R. J., Biancianiello, F., and Shechtman, D., The effect of solidification velocity on the microstructure of Ag-Cu alloy, in *Rapid Solidification Processing Principles and Technologies, III.--Third Conference on Rapid*

- Solidification Processing*, 1982, December, National Bureau of Standards, Gaithersburg, Maryland, 390-396.
110. Beck, D. G., Copley, S. M., and Bass, M., The constitution and phase stability of overlapping melt trails in Ag-Cu alloys produced by continuous laser melt quenching, *Metallurgical Transactions A*, **13A** (1982), 1879-1889.
 111. Walder, S. and Ryder, P. L., Critical solidification behavior of undercooled Ag-Cu alloys, *Journal of Applied Physics*, **74** (1993), 6100-6106.
 112. Embury, J. D., Microstructural aspects of strength and stability of Cu-Ag and Cu-Nb in-situ composites, in *National High Magnetic Field Laboratory Workshop--High-Strength High Conductivity Composite Materials*, 1994, August 18-19, Tallahassee, Florida.
 113. Glazer, J. and Morris Jr., J. W., Thermomechanical processing of two-phase Al-Cu-Li-Zr alloy, in *Aluminum-Lithium Alloys III: Proceedings of the Third International Aluminum-Lithium Conference*, 1986, July 8-11, 1985, University of Oxford, London, 191-198.
 114. Markey, D. T., Biederman, R. R., and McCarthy, A. J., Effect of cold deformation on mechanical properties and microstructure of Alcan XXXA, in *Aluminum-Lithium Alloys III: Proceedings of the Third International Aluminum-Lithium Conference*, 1986, July 8-11, 1985, University of Oxford, London, 173-183.
 115. Cassada, W. A., Shiflet, G. J., and Starke Jr., E. A., The effect of plastic deformation on T_1 precipitation, *Journal de Physique-Colloque C3, supplément au n° 9*, **48** (1987), C3-397-C3-406.
 116. Ashby, M. T., The deformation of plastically non-homogeneous materials, *Philosophical Magazine*, **21** (1970), 399-424.
 117. Embury, J. D. and Fisher, R. M., The structure and properties of drawn pearlite, *Acta Metallurgica*, **14** (1966), 147-159.
 118. Langford, G., Deformation of pearlite, *Metallurgical Transactions A*, **8A** (1977), 861-875.
 119. Spitzig, W. A., Effect of deformation mode on the strength of deformation processed Cu-20%Nb composites, *Scripta Metallurgica*, **23** (1989), 1177-1180.
 120. Lide, D. R., ed. *CRC Handbook of Chemistry and Physics*, 71st ed., , 1990, CRC Press, Boca Raton and Boston.
 121. Elliott, R., *Eutectic Solidification Processing*, 1983, Butterworths & Co Ltd., London.

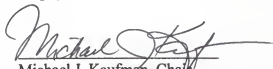
122. Bluni, S. T., Notis, M. R., and Marder, A. R., Nucleation characteristics and microstructure in off-eutectic Al-Zn alloys, *Acta Metallurgica et Materialia*, 43 (1995), 1775-1782.
123. Kuhlmann-Wilsdorf, D., The LEDS theory of strain hardening, in *National High Magnetic Field Laboratory Workshop-- High-Strength High Conductivity Composite Materials*, 1994, August 18-19, Tallahassee, Florida.
124. Von Linde, J. O., Elektrische eigenschaften verdünnter mischkristallegierungen- III. Widerstand von Kupfer- und Goldlegierungen. Gesetzmäßigkeiten der Widerstandserhöhungen, *Annalen der Physik*, 5 Folge, Band 15 (1932), 219-248.
125. Schröder, K., *Handbook of Electrical Resistivity of Binary Metallic Alloys*, 1983, CRC Press Inc., Boca Raton, FL.
126. Shin, M. C., Chung, Y. H., Lee, K. H., Jee, K. K., and Sohn, K. Y., A Study on the Fabrication Process of Al-Li Alloys (IV), MRDD-411-92095, 1992, Agency of Department of Defense, Taejeon, Korea.
127. Benghalem, A. and Morris, D. G., Microstructure and strength of wire-drawn Cu-Ag filamentary composites, *Acta Materialia*, 45 (1997), 397-406.
128. Biselli, C. and Morris, D. G., Microstructure and strength of Cu-Fe in situ composites obtained from prealloyed Cu-Fe powders, *Acta Metallurgica et Materialia*, 42 (1994), 163-176.

BIOGRAPHICAL SKETCH

Keun Yong Sohn was born in Youngdong, Korea, on July 9, 1963. He received his B.E. degree in metallurgical engineering in February 1985 from the Korea University at Seoul, Korea. After that, he entered graduate school at the Korea Advanced Institute of Science and Technology (KAIST) in Seoul, Korea. Under the support of the government of Korea, he completed his M.S. in materials science and engineering in February 1987. After his graduation from KAIST, he joined the Korea Institute of Science and Technology (KIST) in Seoul, Korea, as a research scientist in March 1987 and worked for more than five years in research and development of aluminum alloys. With his outstanding achievements, including two US patents related to the fabrication of aluminum alloys, he awarded the Citation of Excellent Research Scientist from KIST in June 1991.


In pursuing his doctoral study, he again entered graduate school at the Case Western Reserve University (CWRU) in Cleveland, Ohio, in August 1992. After five months at the CWRU, he transferred to the University of Florida, Gainesville. Since January 1993, he has been with the Department of Materials Science and Engineering, University of Florida. After the completion of his doctoral study at the University of Florida in Spring 1997, he will continue to work for his post-doctoral research at the University of Michigan-Ann Arbor.

I certify that I have read this study and that in my opinion it conforms to acceptable standards of scholarly presentation and is fully adequate, in scope and quality, as a dissertation for the degree of Doctor of Philosophy.




Michael J. Kaufman, Chair
Professor of Materials Science
and Engineering

I certify that I have read this study and that in my opinion it conforms to acceptable standards of scholarly presentation and is fully adequate, in scope and quality, as a dissertation for the degree of Doctor of Philosophy.



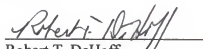
Reza Abbaschian
Professor of Materials Science
and Engineering

I certify that I have read this study and that in my opinion it conforms to acceptable standards of scholarly presentation and is fully adequate, in scope and quality, as a dissertation for the degree of Doctor of Philosophy.



Fereshteh Ebrahimi
Associate Professor of Materials Science
and Engineering

I certify that I have read this study and that in my opinion it conforms to acceptable standards of scholarly presentation and is fully adequate, in scope and quality, as a dissertation for the degree of Doctor of Philosophy.



Robert T. DeHoff
Professor of Materials Science
and Engineering

I certify that I have read this study and that in my opinion it conforms to acceptable standards of scholarly presentation and is fully adequate, in scope and quality, as a dissertation for the degree of Doctor of Philosophy.



Ashok V. Kumar
Assistant Professor of
Mechanical Engineering

This dissertation was submitted to the Graduate Faculty of the College of Engineering and to the Graduate School and was accepted as partial fulfillment of the requirements for the degree of Doctor of Philosophy.

May, 1997



Winfred M. Phillips
Dean, College of Engineering

Karen A. Holbrook
Dean, Graduate School